Biomaterials 328 (2026) 123866

Contents lists available at ScienceDirect

Biomaterials

journal homepage: www.elsevier.com/locate/biomaterials

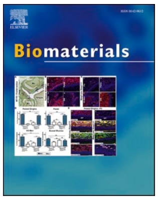

Exploring compartmentalized jet polymerization for novel rod-shaped microgels and their potential in tissue engineering applications

Ninon Möhl[a,b,h], Susan Babu[a,b,i], Camille Bonhomme[b], Ramin Nasehi[a,b], Matthias Mork[a,b], Tamás Haraszti[a,b], Gilles Wittmann[c], Baohu Wu[d], Rostislav Vinokur[b], Kyoohyun Kim[g], Rafael Kramann[e,f], Jochen Guck[g,1], Laura De Laporte[a,b,h,i,*]

[a] *Institute for Technical and Macromolecular Chemistry, RWTH Aachen University, 52074, Aachen, Germany*
[b] *DWI – Leibniz Institute for Interactive Materials, 52074, Aachen, Germany*
[c] *Heinz Maier-Leibnitz Zentrum (MLZ), Technical University of Munich, Lichtenbergstr. 1, Garching, 85748, Germany*
[d] *Jülich Centre for Neutron Science (JCNS) at MLZ, Forschungszentrum Jülich GmbH, Garching, Germany*
[e] *Department of Medicine 2 (Nephrology, Rheumatology, Clinical Immunology, Hypertension), RWTH Aachen University Faculty, Aachen, Germany*
[f] *Department of Internal Medicine, Nephrology, Transplantation, Erasmus Medical Center, Rotterdam, Netherlands*
[g] *Max Planck Institute for the Science of Light and Max-Planck-Zentrum für Physik und Medizin, Staudtstraße 2, 91058, Erlangen, Germany*
[h] *Institute of Applied Medical Engineering, Department of Advanced Materials for Biomedicine, RWTH Aachen University, 52074, Aachen, Germany*
[i] *Max Planck School – Matter to Life (MtL), Jahnstraße 29, 69120, Heidelberg, Germany*

ARTICLE INFO

Keywords:
jet microfluidics
3D cell culture
Rod-shaped microgels
Macroporous hydrogels
Magneto-responsive microgels

ABSTRACT

Anisometric rod-shaped microgels are promising building blocks for tissue engineering, offering injectability, porosity, macroscopic anisotropy, and biochemical functionality—key features for directing cell adhesion, growth, alignment, and interaction. The continuous production of thin or highly porous elongated microgels is therefore desirable, preferably offering control over their stiffness, size, and aspect ratio. We present advancements in compartmentalized jet polymerization, a microfluidic technique that generates microgels that are ten times narrower than the channel width by forming a polymer jet and crosslinking alternating segments with a pulsed laser. Originally limited to diameters of ~8 μm, we have now refined the method to produce microgels as small as ~3 μm. Additionally, we developed ultra-soft and ultra-porous microgels that swell to diameters of 50–120 μm with pore sizes in the range 2–5 μm. While the thin soft microgels can be employed in our Anisogel technology to combine injectability with magnetic alignment, the ultra-porous microgels would increase diffusion in our microporous annealed particle (MAP) scaffolds made from rod-shaped microgels. This paper focuses on the continuous production and characterization of rod microgels with properties that cannot be achieve with other methods. Furthermore, we report initial results of the microgels' potential and challenges to be used inside an Anisogel, which was so far only possible with stiffer magneto-responsive microgels produced by an in-mold polymerization batch process, and to form MAPs by cell-induced assembly of the ultra-porous rods. Further studies will be required to fully exploit the potential of these unique microgels for tissue engineering applications.

1. Introduction

Three-dimensional (3D) microenvironments are essential for tissue engineering because they provide cells with structural support, regulate diffusion, and direct cell-cell interactions. Rod-shaped microgels are powerful building blocks to form 3D microenvironments for tissue engineering, as they are 1000 to 10,000 times larger than the conventional macromolecules used to make hydrogels. The size difference allows them to introduce orientation inside a surrounding hydrogel by magnetic alignment, which is called the Anisogel technology [1–3], or to interlink with each other without a surrounding hydrogel to form microporous annealed particle (MAP) scaffolds with void spaces in

---

This article is part of a special issue entitled: European innovations published in Biomaterials.

[*] Corresponding author. DWI-Leibniz Institute for Interactive Materials, 52074, Aachen, Germany
E-mail address: delaporte@dwi.rwth-aachen.de (L. De Laporte).

[1] Deceased

https://doi.org/10.1016/j.biomaterials.2025.123866
Received 22 April 2025; Received in revised form 14 November 2025; Accepted 20 November 2025

between the microgels of tens to hundreds of micrometers facilitating cell infiltration and migration, and providing more space for cell-cell interactions [4–6].

Despite these advantages, the main challenge lies in the synthesis of rod-shaped microgels with tunable dimensions, mechanics, and compositions. Existing strategies each face trade-offs. Particle replication in non-wetting templates (PRINT) [7] enables the batch production of anisometric microgels down to the micrometer scale but offers little flexibility in stiffness or porosity [1,8]. Plug-flow microfluidics produces rod-shaped microgels with diameters down to ~80 μm in a continuous process, where size is dictated by channel width and post-swelling [9]. A third method, stop-flow lithography (SFL), can achieve rod-shaped microgels with dimensions <10 μm with different shapes, but suffers from limited throughput due to the stop-and-go method [10,11]. Neither approach, therefore, offers the combined control over size, mechanical properties, and compositions needed for anisometric alignment or porous scaffolds formation.

To overcome these limitations, we developed a process known as compartmentalized jet polymerization (CJP) to produce rod-shaped microgels that are ten times narrower than the channel width. This is achieved by generating a thin polymer jet at a four-way junction and spatially controlling photopolymerization with a modulated laser

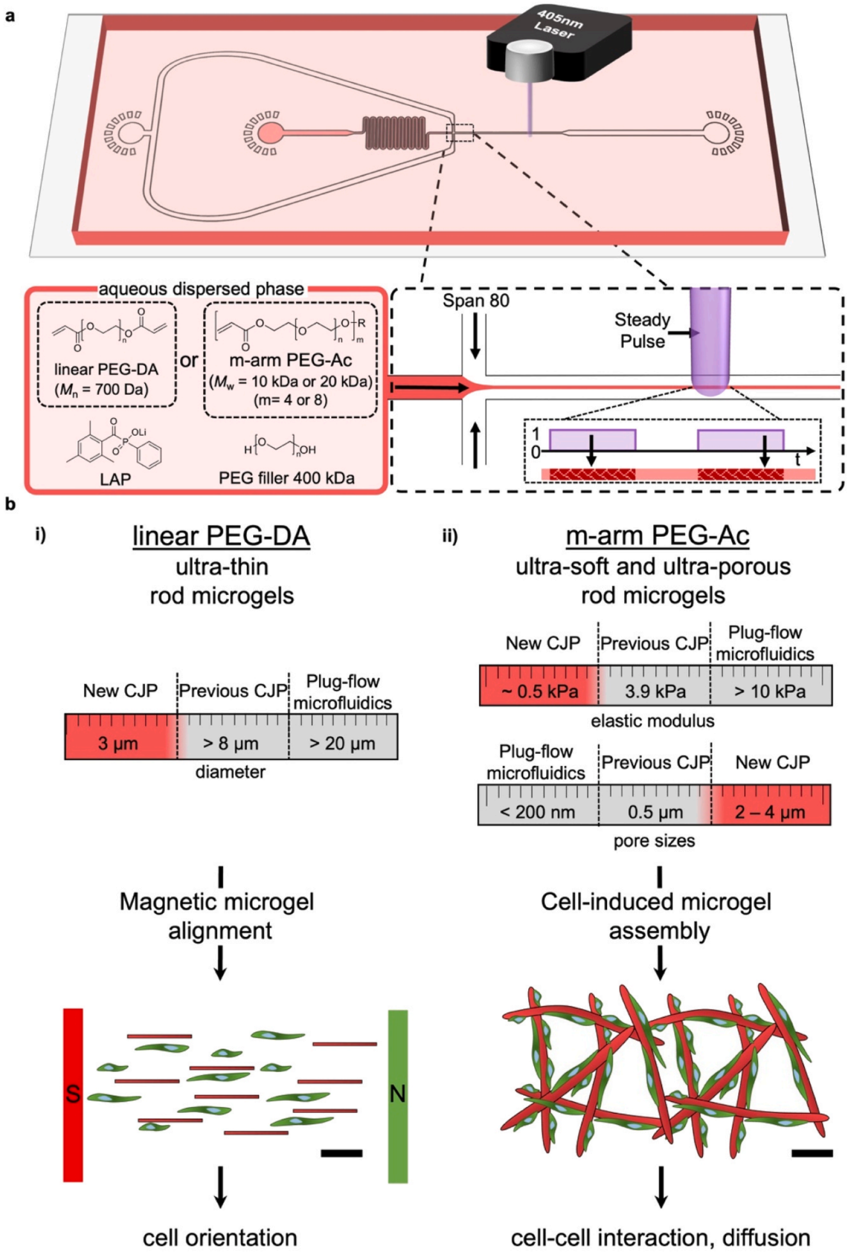

Fig. 1. Overview of the compartmentalized jet polymerization (CJP) method and the types of microgels produced. (a) CJP chip design adapted from Ref. [8]. A time-modulated laser system (wavelength 405 nm) is used to irradiate the polymer jet. Span80 is used as the outer phase and different PEG-based polymers are used as the dispersed phase: (i) PEGDA (700 Da) to produce ultra-thin rod microgels and (ii) four-arm or eight-arm PEG-Ac to produce ultra-soft and ultra-porous rod microgels. The photo-initiator lithium phenyl-2,4,6-trimethylbenzoylphosphinate (LAP) is added to each pre-polymer composition along with a water-soluble PEG filler (PEG-OH, 400 kDa). (b) Two different types of rod microgels (ultra-thin or ultra-soft and ultra-porous) are used for two different tissue engineering applications. The ultra-thin microgels (3–10 μm diameter) are post-functionalized with magnetic particles for cellular alignment, whereas the larger ultra-soft and ultra-porous rod microgels (50–120 μm diameter) are used as building blocks for cell-induced assembly, resulting in large macroscopic pores between the microgels to enhance cell–cell interactions while the microgels enable diffusion.

(Fig. 1a). Hereby, parts of the jet will be crosslinked when the light is on, while others will remain liquid and dissolve after collection. By adjusting parameters such as laser on-time, spot size, and flow rate, the dimensions of the resulting rod microgels can be tuned. Earlier versions of the method demonstrated the potential to produce high-aspect-ratio microgels, but several limitations remained. The rod dimensions were restricted to a minimum diameter of 8 μm using a channel width of 80 μm, and only poly (ethylene glycol) diacrylate (PEGDA) was used as a precursor [8].

In this report, we explored the potential of CJP to produce ultra-thin rod microgels with a diameter of ~3 μm for magnetic alignment (Fig. 1b (i)), or ultra-soft and ultra-porous rod microgels for cell-induced assembly into 3D MAP constructs with large open spaces for cell–cell interaction and sufficient diffusion via the microgel network (Fig. 1b (ii)). These refinements expand the range of accessible rod dimensions, stiffnesses, and porosities, overcoming previous barriers in producing ultra-thin, soft, and porous microgels.

To achieve ultra-thin microgels, the microfluidic design was adapted to enable photopolymerization smaller channels in the presence of atmospheric oxygen. Previous studies have identified oxygen inhibition as a major challenge in producing free radical polymerization (FRP)-based microgels using polydimethylsiloxane (PDMS) microfluidic devices or in forming thin polymer films, since oxygen can diffuse through PDMS and suppress the reaction [12–14]. We observed that simply going smaller in channel geometry did not result in ultra-thin microgels, and while introducing a nitrogen channel helped to remove oxygen, the obtainable size range was still limited. In this work, we present a new approach based on adjusting the channel geometry, which overcomes these limitations and, importantly, eliminates the need for an additional nitrogen chamber. Using this new optimized design, we produced soft (<10 kPa) PEGDA rods with diameters below 5 μm, suitable for post-functionlization with magnetic nanoparticles. This allowed for their magnetic alignment inside an Anisogel and testing the effect of this reduced microgel stiffness on cell alignment, compared to previous Anisogel studies using stiffer (>30 kPa) microgels made by PRINT. To produce larger ultra-soft and – porous microgel rods (50–120 μm diameter), we exploited the brief irradiation times of the high intensity laser and changed the precursor solution to multi-arm star PEGs. Star PEGs introduce more reactive groups, which enabled the production of stable rod-shaped microgels at lower polymer concentrations compared to PEGDA. Physical and mechanical characterization of the rod microgels demonstrated how different precursor molecules alter their structural and mechanical properties. Sufficient free reactive groups were still present in the polymer network after crosslinking to post-modify the microgels with cell-adhesive peptides and triggered cell-induced microgel assembly into 3D cellular assembly. Such constructs form macroscopic pores between the microgels that are densely filled with cells, enhancing the diffusion of nutrients and oxygen via the microgel network and avoiding the formation of necrotic zones [5].

These refinements expand the range of accessible rod dimensions, stiffnesses, and porosities, overcoming previous barriers in producing ultra-thin, soft, and porous microgels. Both the ultra-thin and ultra-soft and -porous rod-shaped microgels address the strong demand for injectable biomaterial building blocks with a multi-phasic structural architecture. Initial experiments in this report demonstrate their ability to provide directional guidance or form MAP scaffolds with macroporosity and enhanced cell–cell interactions in 3D tissue engineering constructs.

2. Results and discussion

2.1. Adjusting the microfluidic design to enable sufficient photopolymerization in the presence of atmospheric oxygen

Molecular oxygen terminates free radical polymerization by reacting with an initiator or growing polymer radicals [15–18]. In bulk solutions, the dissolved oxygen is rapidly depleted, enabling the polymerization reaction to propagate. However, oxygen inhibition becomes predominant when the solution is exposed to an oxygen source. This effect is magnified on the microscale due to the high surface-to-volume ratio [13]. In microfluidics, the chips are usually made from a PDMS elastomer with high oxygen permeability [11,19]. In CJP specifically, oxygen inhibition plays an important role due to the extremely thin jets (surface-to-volume ratio correlates with $1/r$, where r is the radius). The oxygen used during free-radical polymerization is continuously replenished by oxygen diffusing through the microfluidic chip and reaching the continuous oil and aqueous polymer phases flowing inside the microchannels.

The effect of oxygen inhibition became apparent when scaling the microfluidic channel down from 80 μm × 100 μm–25 μm × 25 μm, intending to form an ultra-thin jet for the production of rod microgels with a diameter down to 2.5 μm (one-tenth of the microchannel size). This narrow microgel was shown to be optimal for extensive, oriented neurite outgrowth in a 3D Anisogel system, but so far can only be produced using the PRINT method [20]. Here, we intend to continuously produce microgels with the same dimensions by CJP. Due to the brief irradiation of each microgel to one strong laser pulse, much softer microgels can be obtained compared to the PRINT method that results in anisometric microgels with a Young's modulus of ~35 kPa for a minimum required PEGDA (700 Da) concentration of 10 % (w/v). In contrast to CJP, a larger UV lamp is required in PRINT to expose the entire mold with exposure times >5 min to obtain stable microgels. Therefore, the ability to reproducibly generate ultra-soft and -porous rod microgels is specific to CJP and not accessible by PRINT under comparable conditions. In CJP, we previously used 20 % (w/w) PEGDA (700 Da) as the reactive pre-polymer, mixed with 2.4 % (w/w) of a water-soluble non-reactive PEG filler (400 kDa) and 1 % (w/w) of the photo-initator LAP to form a jet within an 80 μm × 100 μm channel [8].

To achieve stable jetting within a 25 μm × 25 μm channel, the outer phase was adjusted from 100 % Span80 to a 3:1 mixture of Span80 and *n*-hexadecane, reducing the friction force and pressure rise inside the microchannel (Supplementary Information Section 1, Table S1). Although a stable jet was formed, we could not produce ultra-thin rod microgels by CJP within a 25 μm × 25 μm channel, even when testing different polymer concentrations (20–100 % (w/w) PEGDA) or adding more photo-initiator (1–2 % (w/w)) among other measures to increase the reactivity of the jet precursor solution (data not shown).

Reliable photopolymerization during microfluidics has been achieved by limiting the presence of oxygen, for example by degassing [21], nitrogen purging [22], adding oxygen scavengers [23], or confining the reaction to an inert environment [24]. To confirm the effect of oxygen inhibition on free radical polymerization in our system, we designed a chip with a nitrogen channel around the main reaction channel to scavenge unwanted oxygen. The design is based on a previous report [13] and can be found in Supplementary Information Section 2, Fig. S1. We chose a 25 μm × 25 μm channel (does not form microgels in the presence of oxygen) and used 40 % (w/w) PEGDA (700 Da) in the pre-polymer solution. Microgels, 12 ± 1 μm in width and 280 ± 18 μm in length (in the swollen state), could be produced using this setup. The highest possible flow rate to obtain stable microgels using this setup with the 25 × 25 μm channel and nitrogen flow was 65 $\mu L\ h^{-1}$. With a higher flow rate and the formation of a thinner jet, no microgels could be formed. This is likely because the higher flow rates reduced the time of the jet in the irradiation spot, resulting in insufficient crosslinking. Therefore, thinner microgels than 10 μm could not be achieved by adding the nitrogen channel along the smaller channels.

While this strategy confirmed the critical role of oxygen inhibition, such approaches are laborious, not always reproducible, and often impractical in a microfluidic setting. To overcome these limitations, we developed an alternative approach based on channel geometry, which enables reliable microgel production without the need for oxygen-removal steps.

We hypothesized that a larger height-to-width ratio in the microfluidic channel would increase the distance of the center of the jet to the "dead zone" [25]. Accordingly, we changed the dimensions of the microfluidic channel from 25 μm × 25 μm–25 μm × 50 μm or 50 μm × 80 μm (Fig. 2a). Both dimensions were evaluated for their ability to generate ultra-thin microgels with diameters <5 μm using 40 % (w/w) PEGDA (700 Da) as a pre-polymer phase and 3:1 Span80 and *n*-hexadecane. Concentrations of PEGDA <40 % (w/w) did not produce stable microgels using either of the redesigned channels.

The flow rates were varied from 5 to 20 μL h^{-1} for the polymer phase and 100–450 μL h^{-1} for the outer phase, with a maximum of 200 μL h^{-1} within the 25 μm × 50 μm channels and 450 μL h^{-1} within the 50 μm × 80 μm channels (Supplementary Information Section 3, Table S2). Both newly developed channel geometries allowed the production of rod-shaped microgels with minimal diameters of 3 ± 0.8 μm in the swollen state in water after purification (Fig. 2b–e and Supplementary Information Section 4, Fig. S2). The advantage of the 50 μm × 80 μm channel over the 25 μm × 50 μm channel was the handling of the microfluidic device, making it less sensitive to pressure changes. These pressure fluctuations are also reflected by the standard deviations of the obtained microgel dimension (Table 1). The microgel dimensions follow a normal distribution (Supplementary Information Section 4, Fig. S3). While the width of the microgels remains consistens for both channel

Table 1
Microfluidic parameters tested for the production of ultra-thin rod microgels.

Channel dimensions [width, μm × height, μm]	Laser power [mW]	On-time [ms]	Flow rate pre-polymer solution [μL h^{-1}]	Flow rate oil phase [μL h^{-1}]	Microgel dimensions in MilliQ water [width × length, μm]
25 × 50	50	1	5	120	10 ± 1 × 190 ± 18
		0.5	4	150	4 ± 0.2 × 52 ± 5
		1	5	200	4 ± 0.6 × 180 ± 43
50 × 80		1	10	300	7 ± 0.5 × 70 ± 4
		0.50	10	300	7 ± 0.8 × 55 ± 2
		0.25	5	300	3 ± 0.8 × 28 ± 5

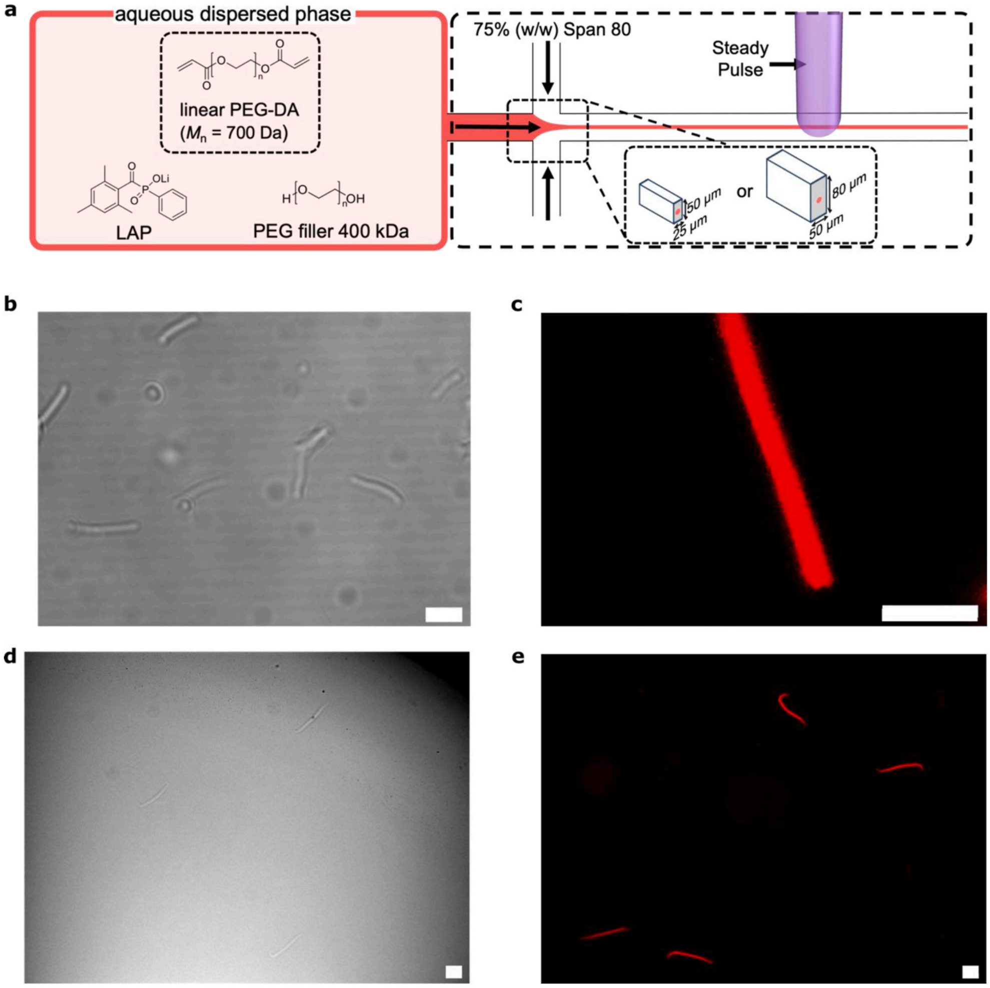

Fig. 2. Representative bright-field and confocal images of microgels produced within rectangular microfluidic channels (50 × 80 μm). (a) Microfluidic channel dimensions to produce ultra-thin rod microgels and pre-polymer used. (b) Microgels 3 ± 0.8 μm in width and 28 ± 5 μm in length, the smallest possible microgel obtained at 5 μL h^{-1} pre-polymer and 300 μL h^{-1} oil flow rates. Scale bar = 20 μm. (c) Confocal images of the same microgels as in (b) labeled with Rhodamine B in red. Scale bar = 10 μm. (d) Bright-field and (e) confocal images of microgels 6 ± 1 μm in width and 122 ± 9 μm in length, labeled with Rhodamine B in red, obtained at 10 μL h^{-1} pre-polymer and 300 μL h^{-1} oil flow rates. Scale bars = 50 μm. Flow rates and irradiation times are summarized in Table 1. (For interpretation of the references to colour in this figure legend, the reader is referred to the Web version of this article.)

geometries, the length varies more in the 25 μm × 50 μm channel than in the 50 μm × 80 μm channel.

2.2. *Analysis of jets by computational fluid dynamic simulation and confocal microscopy*

We used confocal microscopy to study the jet forming inside a 50 μm × 80 μm microfluidic channel and the distances between the polymer jet and the PDMS walls (the oxygen source). Reconstruction of the confocal images revealed a more elongated 3D jet at the crossing section, as well as further down the microfluidic channel (Fig. 3a (i-iii)).

The resulting vertical (*x*–*z*) profile showed that a central jet formed but also an elongated part above the jet in contact with the PDMS surface. The latter may be a real structure or a ghost formed by the strongly fluorescent material in the channel and its reflection from the PDMS–liquid interface above [26]. Analysis of these potential artifacts by laser scanning confocal microscopy was beyond the scope of our study, so we used computational fluid dynamic (CFD) simulations to see if the profiles may depend on the wetting asymmetry of the oil and polymer phases on the glass and PDMS walls.

Fig. 3b–e shows a 3D simulation of jet formation in a 50 μm × 80 μm channel based on the physical properties of the polymer solution and oil phase described above and in Supplementary Information Table S1. More details about the simulation model are provided in Supplementary Information Section 5, Fig. S4 and Table S3. Different contact angles of the polymer phase and the walls were applied during the simulation, such as 180° at the top (PDMS) and bottom (glass), 90° and 90°, 0° and 180°, and 0° and 0°. The contact angles of the oil phase were then calculated as 180° minus the contact angle of the polymer phase. The first condition (180° at the top and bottom), where a focused cylindrical jet is formed (Fig. 3b), was anticipated inside the microfluidic channel because we applied a hydrophobic coating. However, confocal images suggested a different flow profile. This may be explained by the simulations indicating that two contact angles of 90° (Fig. 3c) or contact angles of 0° and 180° (Fig. 3d) lead to more elongated jets. The last condition (0° at the top and bottom; Fig. 3e) is the least likely. Importantly, the produced microgels were cylindrical and much thinner than the cross-section of the polymer phase predicted by the simulation results in Fig. 3c (~22 μm in diameter). This finding, together with the fact that the smallest microfluidic channel (25 μm × 25 μm) could not produce rod microgels, again suggests that the jet may not be polymerized over its entire height when briefly exposed to light and in contact with oxygen. These observations indicate that a "dead zone" existed due to the presence of oxygen adjacent to the PDMS top wall inside the channel where free radical polymerization does not occur during CJP, and that this dead zone likely overlaps partially with the jet.

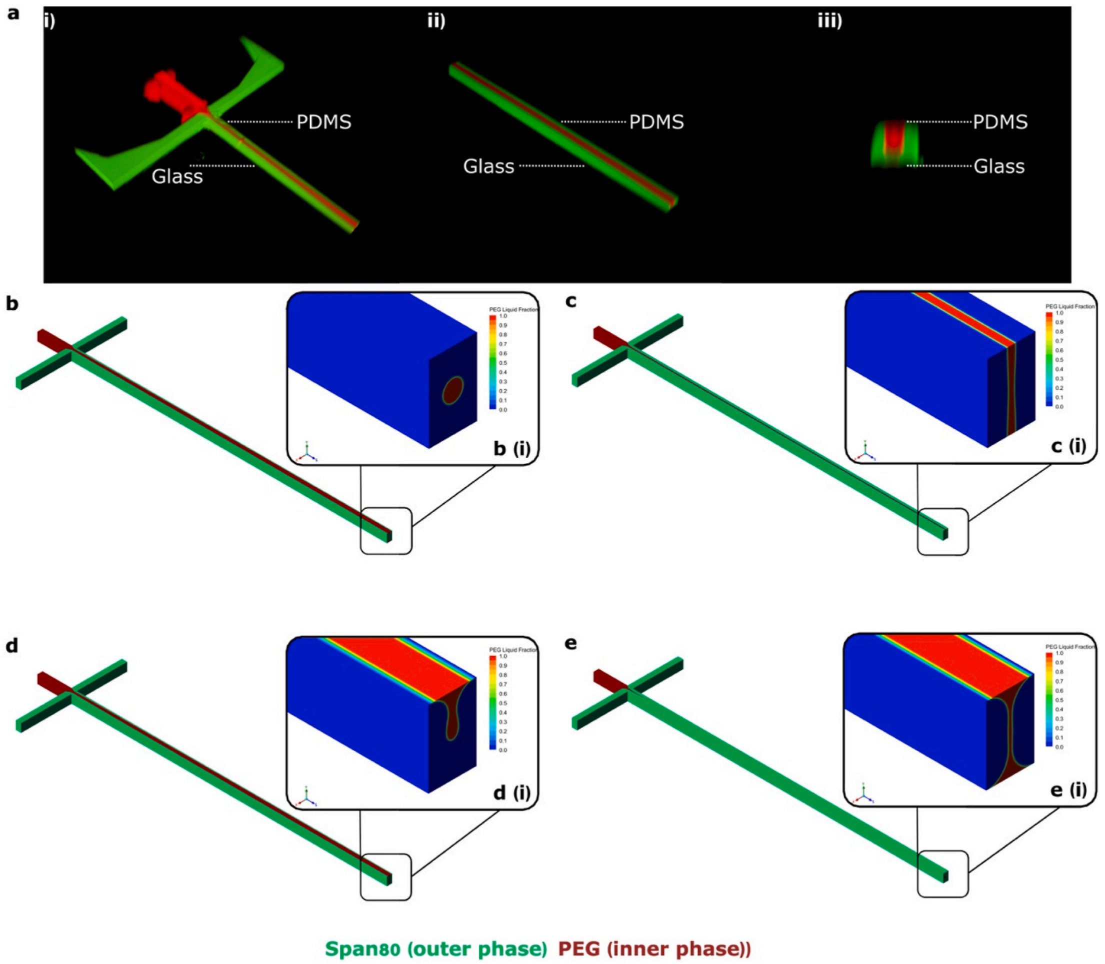

Fig. 3. Formation of a 3D jet in the 50 × 80 μm microchannel chip. (a) Confocal images showing the formation of a 3D jet, captured along different regions of the flow such as (i) near the T-junction where flow focusing occurs, (ii) and (iii) further down the jet where light irradiation takes place (inner phase = pre-polymer in red; outer phase = Span80 in green). (b–e) The results of a simulation model with different contact angles of the inner pre-polymer phase at the top (PDMS) and bottom (glass) walls of microchannel: (b) 180°–180°, (c) 90°–90°, (d) 0°–180° and (e) 0°–0°. (For interpretation of the references to colour in this figure legend, the reader is referred to the Web version of this article.)

2.3. *Magnetic alignment of ultra-thin rod-shaped microgels inside 3D anisogels*

The 40 % (w/w) PEGDA ultra-thin rod microgels were magnetized with superparamagnetic iron oxide nanoparticles (SPIONs), as previously reported for PRINT microgels [7,20]. For PRINT microgels, only 1.8 μg mL^{-1} of SPIONs (<10 μM iron) was required to orient the microgels in ~20 s due to their high aspect ratio. In multiple studies [1,10,27,28], the magnetization of rod microgels was achieved through the addition of the nanoparticles to the pre-cursor solution. However, in CJP, this approach did not prove to be suitable (Supplementary Information Section 6 and 7, Figure S5 and S6, Table S4, Supplementary Video 1 and 2) due to insufficient and heterogeneous functionalization.

To achieve a more homogenous SPION distribution, we coupled the SPIONs to the microgel network after production instead of mixing them with the precursor solution before crosslinking. To achieve this, we used custom-made magnetic nanoparticles (~70 nm diameter) with a non-ionic PEG-methacrylate (PEGMA) surface coating, which can chemically couple to unreacted free acrylates of the microgel network via free-radical polymerization. A previous study has demonstrated that surface-magnetized solid rods can orient in very weak magnetic fields (1–10 mT) [29], with a mathematical model suggesting that surface-magnetized solid rods require a 69 % weaker magnetic field than anisotropic elements with magnetic nanoparticles throughout their entire volume. Such an approach could, therefore, also allow for a decrease in nanoparticle concentration. To post-functionalize the microgels with SPIONs, a solution consisting of 1 % (w/w) LAP, PEGMA SPIONs and microgels was exposed to a self-constructed light emitting diode (LED) in the UV range ($\lambda = 365$ nm, spot diameter ~4.7 mm, ~135 mW cm^{-1}) for 10 min. To investigate the impact of the aspect ratio (AR) on the required amounts of nanoparticles to align the microgels, we compared microgels with a diameter of 10 μm and aspect ratios of 15, 19 or 30. After purification, the magnetic response of the microgel rods was tested in water using a weak magnetic field (~70 mT). Different concentrations of magnetic nanoparticles (200–600 μg ml^{-1} with respect to the total volume of the microgels) were incubated with the microgels (Fig. 4a, Supplementary Videos 3–5). We found that a SPION concentration of 200 μg ml^{-1} was sufficient for higher aspect ratios (19, 30), whereas 600 μg ml^{-1} was required for lower aspect ratios (15), to magnetically align the microgels in ~3 s.

After sufficient time for complete alignment, the degree of alignment was quantified by determining the full width half maximum (FWHM) of the histogram depicting the angles of microgel orientation in relation to the magnetic field lines (Fig. 4b). We assumed satisfactory alignment when the FWHM was <90° [1,20]. Only the SPION concentration of 600 μg ml^{-1} achieved a sufficiently low FWHM for all aspect ratios, but microgels with an aspect ratio of 30 also oriented at lower SPION concentrations. We did not expect microgels with a lower AR (15) to require a higher SPION concentration for alignment because in the case of PRINT microgels, the shorter PRINT microgels rotate more rapidly (AR of 2.5 compared to 20 for a microgel width of 10 μm) [30]. Even though longer aspect ratios result in a higher magnetic driving force, the viscous torque of higher aspect ratios normally increases more strongly than the magnetic torque, counteracting the rotation. This may not be the case for CJP microgels as these are now much softer than the PRINT microgels (~2 kPa vs 35 kPa), suggesting a higher porosity and thus reduced viscous torque. Furthermore, SPIONs on the outside of the microgels likely increase the magnetic torque compared to interstitial SPIONs. We were unable to fully align rods with diameters of 3–4 μm and lengths of 25–50 μm in water (Supplementary Information Section 8, Fig. S7). This might be due to their smaller aspect ratio or microgel clustering during centrifugation. Making ultra-thin rod microgels with longer AR resulted in bending of the microgels during production due to the low Young's modulus. The lowest possible AR to align microgels with a diameter of 10 μm was 13 with post-functionalization in 600 μg ml^{-1} of PEGMA-coated SPIONs.

As we aim to reduce the amount of synthetic material, we selected these rods to investigate whether cellular alignment is possible with CJP-produced microgels inside the Anisogel. In addition, we observed in unpublished work alignment of cells using PRINT microgels with a width of 10 μm and length of 100 μm (AR of 10). The CJP microgels (AR: 13) were added to the PEGKQ precursor solution (~1 % (v/v)) and 600 μM of the cell-adhesion peptide GRGDSPC together with mouse L929 fibroblasts (700 cells/μL). These microgels were much softer (Young's modulus ~2 kPa, Fig. 4c) than the PRINT microgels used in previous studies with a minimum Young's modulus of 35 kPa [1]. With the PRINT technique, a minimum irradiation time of 5 min is required to achieve stable particle production when using the standard PEGDA concentration of 20 % (w/w) (Supplementary Information Section 9, Fig. S8). Instead, increasing the concentration to 40 % (w/w), as we do with CJP, enables stable fabrication with an irradiation time as short as 1 s. However, even with this short irradiation time, the resulting microgels still exhibited a Young's modulus of 413 ± 45 kPa, measured by colloidal AFM — which is approximately 200-fold higher than what can be achieved using the CJP method (Supplementary Information Section 9, Fig. S8). As the surrounding 1.25 % (w/v) PEGKQ hydrogel only has a storage modulus of ~10 Pa, the PRINT microgels lead to large differences in stiffness between the microgels and the surrounding gel. Using the much softer CJP-produced microgels, we determined whether cells still experience sufficient mechanical anisotropy to grow in a unidirectional manner following the aligned microgels. The samples were incubated for 7 days and the orientation of the cells was assessed by confocal microscopy and quantitative image analysis. The fibroblasts showed more growth in the direction of the aligned microgels (Fig. 4d) but only seemed to align when close to a microgel (Fig. 4e). In comparison, the control with randomly oriented microgels showed no cellular alignment (Fig. 4f). Quantification of the microgel alignment by calculating the FWHM of the angle distribution (Fig. 4g) revealed that the FWHM was <90° for the microgels but higher for the cells (FWHM >90°) compared to our previous studies using PRINT microgels. This suggests that the stiffness difference of the microgels and the surrounding hydrogel plays an important role in terms of cellular guidance. Less mechanical anisotropy may be sensed by the cells because the CJP-produced microgels are ~20-fold softer than the PRINT microgels. To compensate for this effect, we may need to use longer or stiffer microgels or a higher microgel concentration, which will be tested in a follow-up study. The ability to produce softer rod microgels and render them magnetic makes it now possible to study important biomechanical questions, such as the stiffness threshold of the rods with respect to the surrounding hydrogel matrix, to induce cellular alignment. This is especially important when mimicking different native tissues, as we can study the required mechanical guidance cues depending on the cell types. More information on the quantification of the FWHM can be found in Supplementary Information Section 10.

2.4. *Production of ultra-porous and ultra-soft rod-shaped microgels*

Conventional polymer networks, specifically those in synthetic hydrogels [31] and microgels [32], typically possess nanometer-sized pores. However, such pore sizes do not always support sufficient diffusion of macromolecules for tissue engineering. Several techniques have been developed to introduce microporosity and macroporosity into hydrogels [33] and microgels [34]. For example, pH-degradable monodisperse supramolecular nanogels have been used as a sacrificial colloidal template to produce microgels containing pores of 300–360 nm [34]. Unlike methods that require sacrificial templates, CJP achieves high porosities mainly due to the short irradiation time and the low conversion of the polymer network, rendering the microgels intrinsically porous. The addition of unreactive filler molecules to stabilize the jet may also contribute to porosity by inducing phase separation during free-radical gelation, followed by the removal of the non-reacted phase during purification [7,8,35].

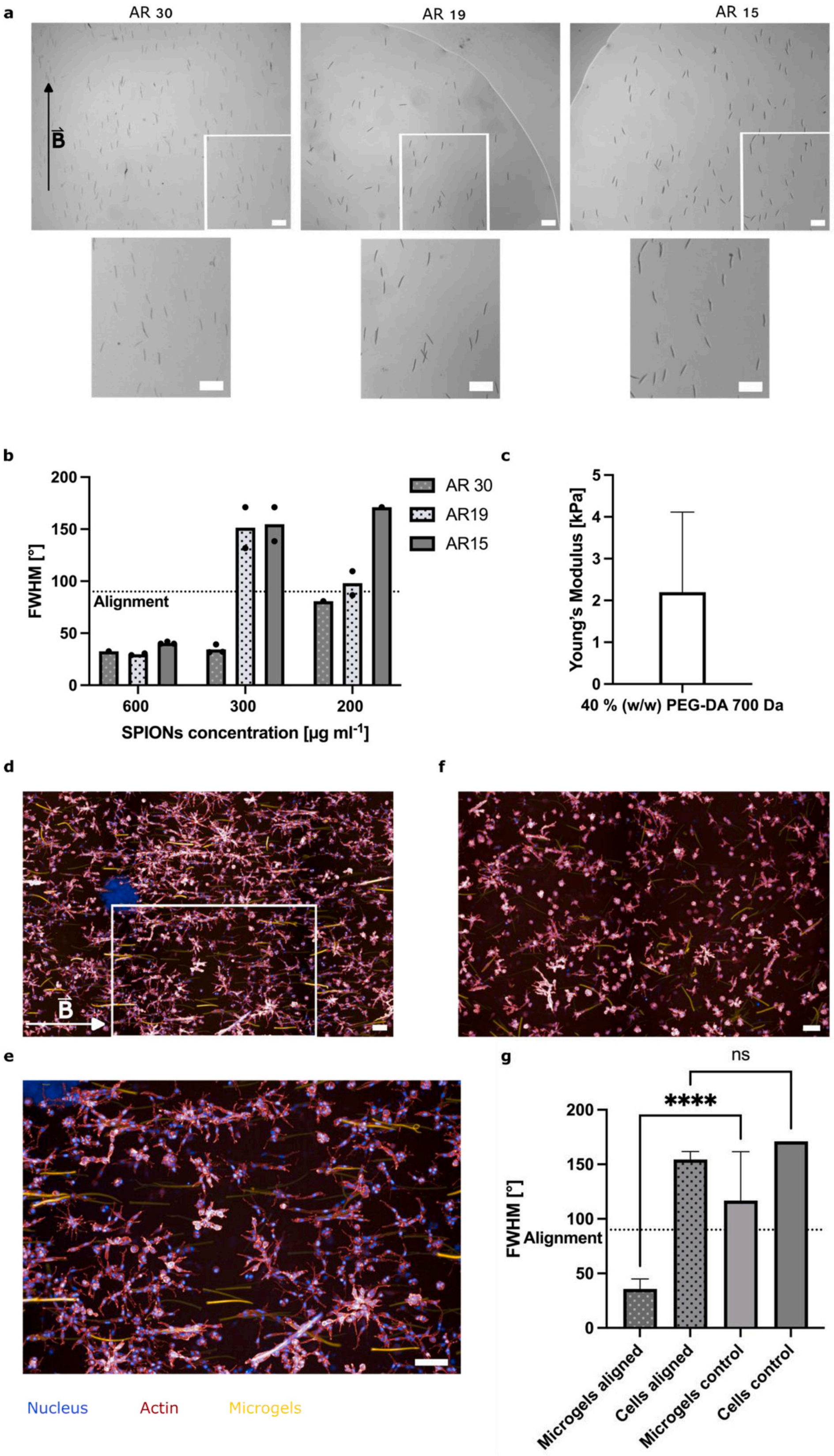

(caption on next page)

Fig. 4. CJP microgel and cell alignment. (a) Alignment of post-functionalized rod microgels with PEGMA SPIONs featuring different aspect ratios (AR = 30, 19, or 15) in water with the highest SPION concentration of 600 μg ml^{-1}. The arrow indicates the direction of the magnetic field (70 mT). White boxes indicate magnification of the images placed below. Scale bars = 200 μm. (b) Image analysis to quantify the FWHM of microgels containing different amounts of PEGMA SPIONs and featuring different aspect ratios. Alignment is satisfactory when FWHM <90°. (c) Young's modulus of 40 % (w/w) PEGDA thin rod microgels measured by colloidal AFM. (d) Anisogel preparation with L929 mouse fibroblasts (700 cells μL^{-1}) (red) and post-functionalized magneto-responsive rod-shaped microgels (10 μm × 130 μm) with 600 μM GRGDSPC inside a PEGKQ matrix, cultured for 7 days. The white arrow indicates the magnetic field direction for all images. Scale bar = 100 μm. (e) Magnified image of fibroblasts growing inside the Anisogel. The magnified region is bounded by the white box in image (d). Scale bar = 100 μm. (f) Control L929 mouse fibroblasts (700 cells μL^{-1}) (red) cultured in randomly oriented post-functionalized magneto-responsive rod-shaped microgels. Scale bar = 100 μm. (g) Image analysis to quantify the FWHM of microgel and cell alignment inside hydrogels with aligned (Anisogel) and unaligned (control) microgels. Alignment is satisfactory when FWHM <90°. Data are means ± standard errors. Statistical significance was determined by one-way ANOVA with Tukey's multiple comparison test (*$p < 0.5$; **$p < 0.01$; ***$p < 0.001$; ****$p < 0.0001$). (For interpretation of the references to colour in this figure legend, the reader is referred to the Web version of this article.)

We exploited brief irradiation (milliseconds to seconds) to produce ultra-porous and ultra-soft microgels. Short irradiation times combined with oxygen inhibition generate polymer networks with low conversions [8]. This leads to softer CJP rod microgels that swell more than PRINT microgels based on the same polymer concentrations. Previously, pore sizes of ~510 nm have been reported for CJP microgels prepared from 20 % (w/w) PEGDA (700 Da) compared to ~110 nm for equivalent PRINT microgels [8]. Softer and more porous rod microgels are useful for tissue engineering due to their superior diffusion properties and similar mechanical behavior to soft native tissues such as the brain. This is particularly important when rod-shaped microgels are interlinked to form 3D MAP scaffolds. When cells grow and fill the free space between microgels, the microgel network can support the cells with a better diffusion of oxygen and nutrients. This inhibits the formation of a necrotic core and supports the growth of larger tissues. MAP scaffolds have thus far been prepared using rod-shaped or spherical microgels with elastic moduli >10 kPa and mesh sizes in the nanometer range [5,6,36].

To test the effect of the molecular structure of the reactive polymer on the microgel network and its stiffness, we compared the linear PEGDA precursor to multi-arm star PEG-acrylates (sPEG-Ac) when crosslinked by free radical polymerization using 1 % (w/w) LAP. Four star polymers were tested: four-arm sPEG-Ac 10 and 20 kDa, and eight-arm sPEG-Ac 10 and 20 kDa (Supplementary Information Section 11, Table S5). Before performing the microfluidic experiments, we determined the gelation times and storage moduli of bulk hydrogels prepared from all reactive polymers at a concentration of 5 % (w/w) using rheology (Fig. 5a–c). The softest gel was achieved using linear PEGDA (0.6 ± 0.1 kPa), in line with our previous observations [37]. This supports the hypothesis that sPEG-Ac generates denser and more stable networks than PEGDA. Although a shorter, linear molecule has more reactive groups for the same weight concentration than four- or eight-arm branched molecules with a higher molecular weight, larger molecules take up a higher volume, facilitating the reactive groups to interact with each other. On the other hand, for both sPEG-Ac structures, the gelation time tends to increase with molecular weight, likely because there are fewer reactive groups available at a constant weight concentration (Fig. 5c). Even so, the 20-kDa four-arm sPEG-Ac produced a hydrogel with a lower storage modulus (10.6 ± 0.8 kPa) than its 10-kDa equivalent (11.9 ± 0.04 kPa), whereas the 20-kDa eight-arm sPEG-Ac produced a hydrogel with a higher storage modulus (14.5 ± 0.8 kPa) than its 10-kDa equivalent (5.6 ± 0.08 kPa). The unexpected latter result may reflect the high coil density of the 10-kDa eight-arm sPEG-Ac, making the reactive groups less available [37]. Similarly, the storage moduli of hydrogels prepared from 10-kDa eight-arm sPEG-Ac were much lower than those prepared from four-arm sPEG-Ac despite the extra arms providing additional reactive acrylate groups.

Given that bulk hydrogels prepared from multi-arm polymers have higher storage moduli than those prepared from linear PEGDA, we tested the use of sPEG-Ac in CJP to determine whether this polymer architecture yields stable microgels at polymer concentrations below 20 % (w/w), aiming to reduce the amount of synthetic material. The four different sPEG-Ac variants and PEGDA were each mixed with PEG filler (400 kDa) and 1 % (w/w) LAP, and were used as the dispersed phase in an 80 × 100 μm microfluidic chip (Fig. 5d). Pure Span80 was used as the continuous phase. Interestingly, under these conditions, a minimum jet width of 30 μm was required to obtain stable microgels. All rod microgels were produced at the same flow rates of 50 μL h^{-1} for both the dispersed and continuous phases, with laser on-times of 50 ms at a frequency of 10 Hz. The lowest polymer concentrations that produced stable microgels were 3 % (w/w) for 20-kDa eight-arm sPEG-Ac, 5 % (w/w) for 10-kDa eight-arm sPEG-Ac, 8 % (w/w) for four-arm sPEG-Ac (10 or 20 kDa), and 20 % (w/w) for PEGDA (700 Da). The lowest concentration of 3 % (w/w) matched the rheological data, where 20-kDa eight-arm sPEG-Ac showed the highest storage modulus at a given prepolymer concentration. The low concentration of 5 % (w/w) for 10-kDa eight-arm sPEG-Ac was more surprising because this resulted in the lowest storage modulus of all bulk hydrogels prepared from sPEG-Ac. This may reflect the difference in exposure time between CJP and rheology, because a larger number of arms may be more important than chain mobility in the formation of stable microgel networks during short irradiation times.

The Young's moduli of the microgels as determined by atomic force microscopy (AFM) are shown in Fig. 5e. For the four-arm sPEG-Ac at 8 % (w/w), the reactive polymers produce microgels with Young's moduli of 1.1 ± 1.6 kPa and 0.30 ± 0.1 kPa for the 10 and 20 kDa variants, respectively, in agreement with the bulk hydrogel rheology data. Microgels prepared from 5 % (w/w) eight-arm sPEG-Ac (10 kDa) had a Young's modulus of 0.6 ± 0.5 kPa, whereas those produced from 3 % (w/w) eight-arm sPEG-Ac (20 kDa) had a Young's modulus of 1.2 ± 0.2 kPa. To our knowledge, this is the first report of such soft, rod-shaped microgels. In contrast, the microgels prepared from 20 % (w/w) linear PEGDA had a Young's modulus of 2.5 ± 1.2 kPa.

The pore size of the soft microgels was investigated by confocal microscopy and image analysis (Fig. 5f and Supplementary Information Section 12, Fig. S9). The softest microgels, prepared from 8 % (w/w) four-arm sPEG-Ac (20 kDa), also featured the largest pores, ranging from 1 to 5 μm in diameter and accounting for ~94 % of the area occupied by pores. The equivalent microgels prepared from 8 % (w/w) four-arm sPEG-Ac (10 kDa) featured pores mostly ranging from 1 to 3 μm in diameter and accounting for 66 % of the area occupied by pores. For microgels prepared from the eight-arm sPEG-Ac variants at the lowest possible concentrations (5 % (w/w) for the 10-kDa variant and 3 % (w/w) for the 20-kDa variant), most pores were 1–3 μm in diameter and accounted for 96 % or 84 % of the area is occupied by pores, respectively. For all microgels, we found a uniform distribution of the pore size across the z-direction of each microgel (Supplementary Information Section 12, Fig. S9). This is concordant with the mechanical properties, where 20-kDa eight-arm sPEG-Ac produced the stiffest microgels. All ultra-porous and ultra-soft rod microgels had diameters exceeding 50 μm due to the minimal required jet widths of ~30 μm. Producing thinner ultra-porous and ultra-soft microgels is hindered by the high ratio of stabilizing non-reactive filler to reactive PEG.

To investigate the influence of the precursor molecules on the mechanical and structural properties of the ultra-soft and ultra-porous rod-shaped microgels in more detail, we set the polymer concentration to 10

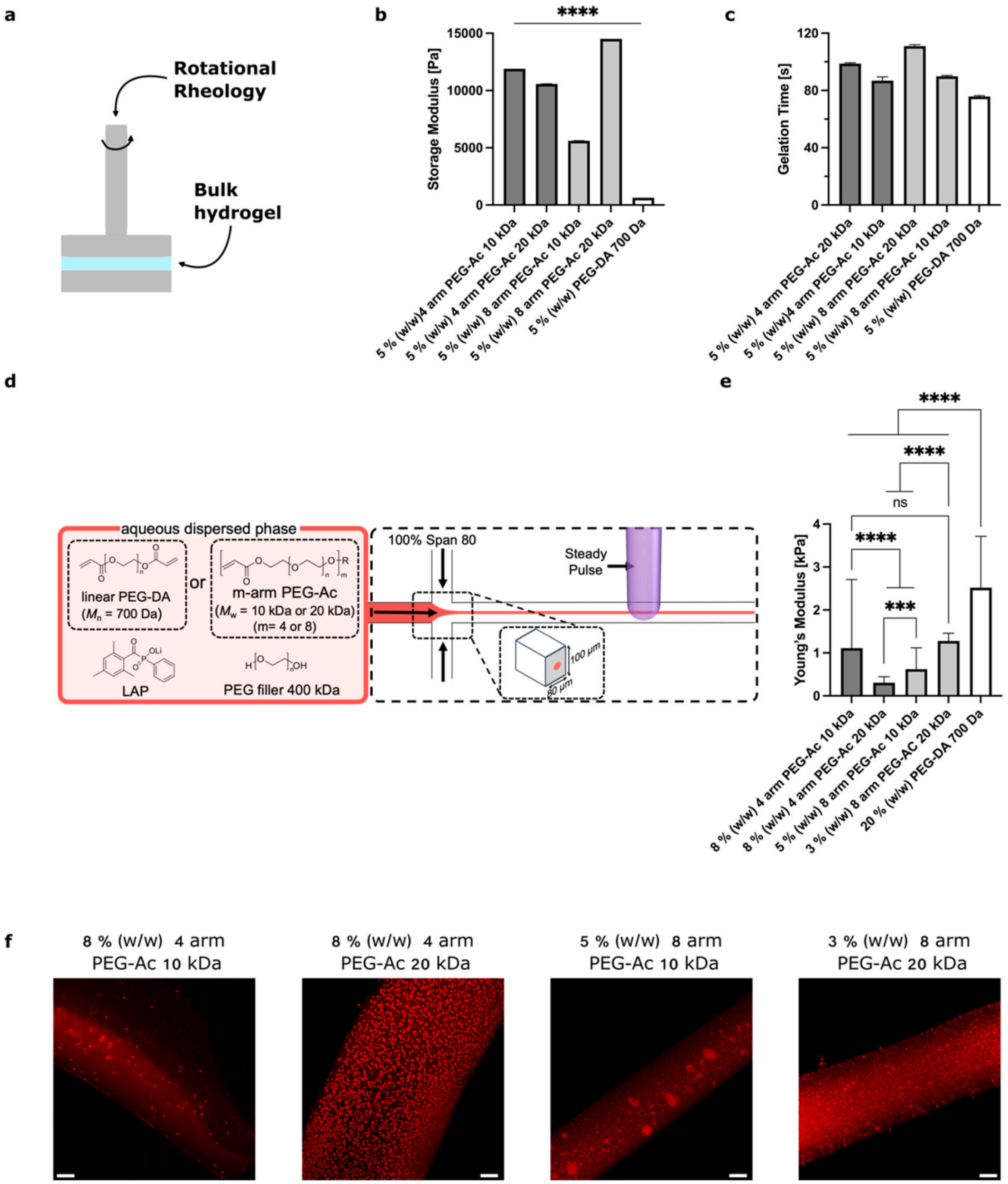

Fig. 5. Mechanical properties of ultra-soft microgels. (a) Rotational rheology set up of bulk hydrogels to measure (b) the storage modulus and (c) the gelation time. (d) Microfluidic set up with channel dimensions and pre-polymer used to produce ultra-soft microgels. (e) Young's modulus of rod shaped microgels with the lowest possible polymer concentration and different precursors in CJP. Data are means ± standard errors ($n \geq 3$). Statistical significance was determined by one-way ANOVA with Holm-Sidak's multiple comparisons test (b) and one-way ANOVA with Tukey's multiple comparisons test (e) (*$p < 0.5$; **$p < 0.01$; ***$p < 0.001$; ****$p < 0.0001$). (f) Porosity analysis of rod microgels (red). Scale bars = 15 µm. Displayed images were processed for better visibility (background removed) but porosity analysis was applied to raw images (Fig. S9). (For interpretation of the references to colour in this figure legend, the reader is referred to the Web version of this article.)

% (w/w) for all sPEG-Ac variants and to 20 % (w/w) for PEGDA to ensure stable microgel production, and analyzed the microgels by colloidal AFM, Brillouin microscopy, optical diffraction tomography (ODT), and small angle X-ray scattering (SAXS). First, the Young's moduli of the microgels were determined by colloidal AFM (Fig. 6a). For sPEG-Ac, the stiffest microgels were produced from 20-kDa eight-arm sPEG-Ac, resulting in a Young's modulus of 1.6 ± 1.3 kPa, whereas the 20-kDa four-arm sPEG-Ac was the least stiff (0.5 ± 0.2 kPa). ODT and Brillouin microscopy were used to characterize the mechanical properties of the microgels in more detail (Fig. 6b and c and Supplementary Information Section 13, Fig. S10). The refractive index (RI) is proportional to the mass density of the sample and suggested a lower density for four-arm samples compared to eight-arm samples. Microgels prepared from 20-kDa four-arm sPEG-Ac had the lowest RI, in agreement with the lowest measured Young's modulus, indicating that these samples contain the most water. However, the Brillouin frequency shift, which is related to the longitudinal modulus (the inverse of compressibility) [38] of the microgels, showed a different trend. Usually, a higher Brillouin frequency shift is expected for samples containing less water with higher Young's moduli or higher RI. The higher Brillouin frequency shift of four-arm compared to eight-arm sPEG-Ac microgels, regardless of the molecular weight, was therefore unexpected (Fig. 6c). Higher

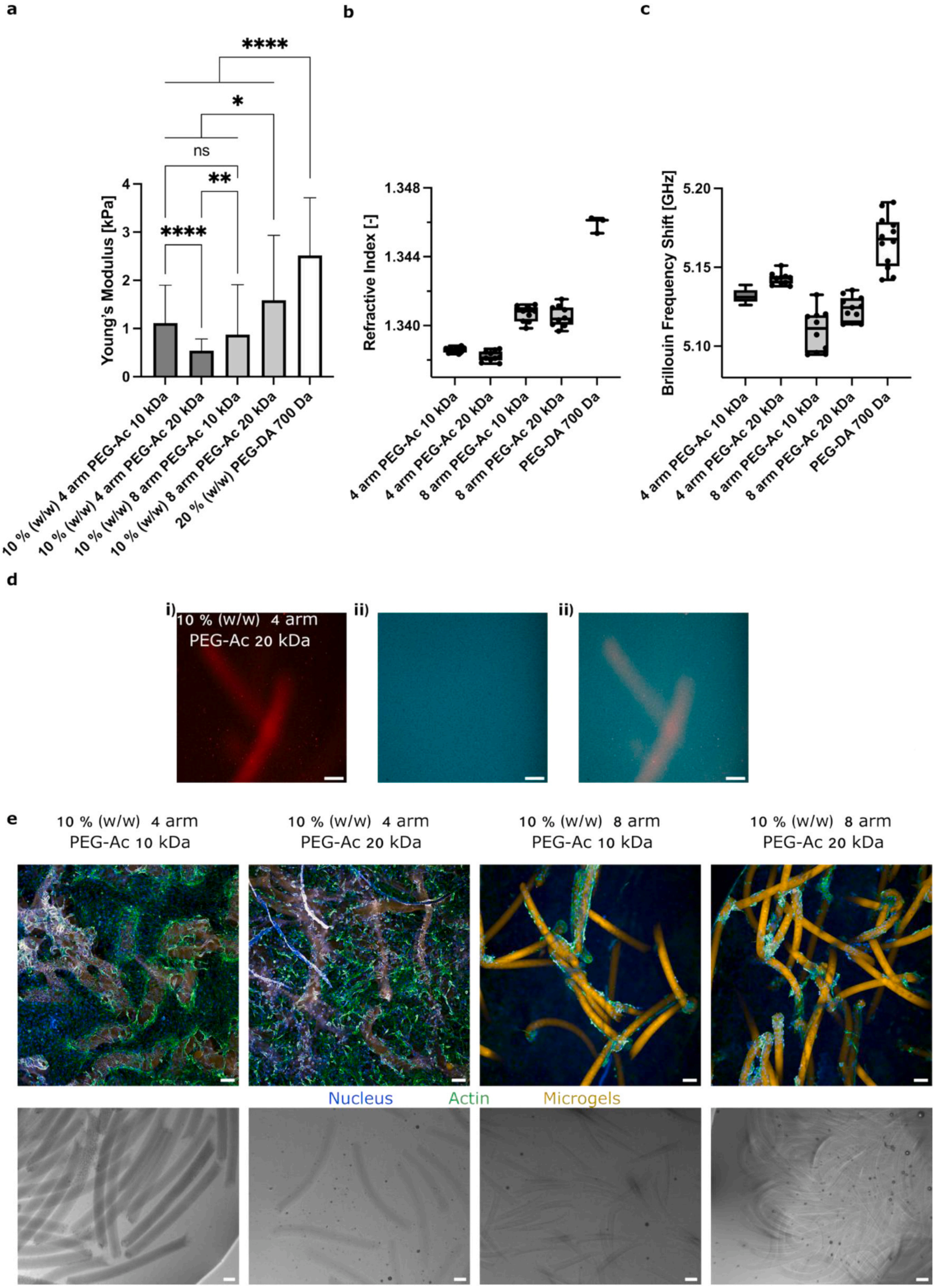

Fig. 6. Mechanical and structural properties of rod microgels prepared from multi-arm sPEG-Ac (10 % (w/w)) and linear PEGDA (20 % (w/w)) and cell-microgel interaction. (a) Young's modulus determined by atomic force microscopy (AFM). (b) Refractive index. (c) Brillouin frequency shift. Data are means ± standard errors. Statistical significance was determined by one-way ANOVA with Tukey's multiple comparisons test (*$p < 0.5$, **$p < 0.01$, ***$p < 0.001$, and ****$p < 0.0001$). (d) Diffusion experiment using FITC-dextran 500 kDa and 10 % (w/w) 4 arm PEG-Ac 20 kDa microgels. Confocal images of the rhodamineB (red) labeled microgels (i) inside a water-based solution of 0.05 mM FITC-dextran (blue) showing the immediate diffusion of the fluorescently labeled dextran into the microgels as the contours of the microgels are not visible (ii). Merged both channels (iii). Scale bars are 100 μm. (e) Cells interact differently with four- and eight-arm sPEG-Ac. Bright-field images of 10 % (w/w) rod microgels with different multi-arm sPEG-Ac (top) and interactions between L929 fibroblasts (200 μL^{-1}) on respective GRGDSPC-functionalized rod microgels (bottom). Scale bars = 100 μm. (For interpretation of the references to colour in this figure legend, the reader is referred to the Web version of this article.)

storage moduli of nanocomposite hydrogels with lower Brillouin moduli have previously been attributed to their characterization at different length scales [39]. Whereas Brillouin microscopy focuses on a local area of the sample, the storage or Young's moduli describe stiffness at the macroscopic scale. Therefore, these observations suggest more heterogeneous mechanical properties at smaller length scales. In the case of nanocomposite hydrogels, this may reflect the addition of nanoparticles, whereas in our microgels the highly porous network might be the cause for this heterogeneity, with the eight-arm sPEG-Ac microgels leading to more heterogeneous networks due to their small coil sizes.

The nanostructures of 10 % (w/w) sPEG-Ac and 20 % (w/w) PEGDA microgels were also analyzed by SAXS (Supplementary Information Section 14, Fig. S11). The scattering patterns of the four sPEG-Ac samples differed significantly in the high-q region due to variations in polymer chain conformation. Specifically, a correlation peak near $q = 0.2\ \text{Å}^{-1}$ was most prominent for the 20-kDa four-arm sPEG-Ac, probably reflecting local domains where the arm chains accumulate and stacking, resulting in a more ordered structure. Such domains indicate unreacted polymer arms and are in line with the low Young's modulus for these samples. More information on the SAXS method and models are provided in Supplementary Information Section 14.

In a previous paper where nanoporous microgels were produced with plug-flow microfluidics [37], we demonstrated limitations in diffusion of fluorescently labeled dextrans depending on their size and the properties of the prepolymer solution. With the micrometer range pores of the ultraporous CJP microgels, we would have unhindered diffusions of larger growth factors and other proteins, like chondroitinase ABC (~121 kDa), which is known to degrade scar tissue after spinal cord injury. To assess the potential of enhanced diffusion using sPEG-Ac CJP microgels, we incubated the softest microgels with 10 % (w/w) 4 arm sPEG-Ac 20 kDa with fluorescently labeled dextran (FITC-dextran, 500 kDa) (Fig. 6d). This dextran exhibits a stokes radius of 14.7 nm, being larger than the previously probed sizes of 2.3–6 nm [37]. We recorded confocal images of the Rhodamin B labeled microgels prior (Fig. 6d (i)) and right after mixing the microgels with the dextran solution (Fig. 6d (ii)), showing the immediate diffusion into the microgels, as the contours of the microgels are not visible (Fig. 6d (iii)). Therefore, we believe that the ultraporous CJP microgels have a high potential as building blocks of MAP scaffolds.

To study the ability of cells to adhere and spread onto the microgels, microgels prepared with 10 % (w/w) of the four sPEG-Ac variants were biofunctionalized with a cell-adhesion peptide (GRGDSPC) post-production (1 mM with 22 microgels per microliter) before seeding with mouse L929 fibroblasts (12 microgels and 200 cells per microliter). The rod microgels were 50–120 μm in width and 600–1000 μm in length. After cultivation for 7 days, the cells behaved very differently on microgels prepared from four-arm compared to eight-arm sPEG-Ac (Fig. 6e). Cells on the four-arm sPEG-Ac microgels mostly interacted with each other and the well surface, forming a monolayer into which the rod microgels were incorporated. In contrast, cells attached to the eight-arm sPEG-Ac microgels, which remained separated with a few microgels stacked on top of each other. As the four-arm and eight-arm sPEG-Ac resulted in similar Young's moduli, the different cellular interaction is likely not caused by the stiffness. It rather suggests a link between the RI and cell interaction. A higher RI in the case of the eight-arm sPEG-Ac microgels may be caused by a more heterogeneous polymer network, which could lead to a less homogenous distribution of the cell adhesive RGD peptide after post-functionalization. It has been demonstrated before that there is a maximum distance (~60 nm) between RDG peptides on hard substrates for cells to be able to form focal adhesions [40]. Besides differences in RGD distances, the total amount of RGD coupled to the microgels and their mobility would also impact cell behavior [41]. As the accessibility of remaining acrylates to functionalize with cell adhesive peptides might be impaired due to the higher coil like structure with respect to the 8 arm sPEG-Ac microgels, this could lead to a lower concentration of RGD ligands on the surface of the microgels leading to the observed reduction in cell spreading.

We then determined whether fibroblasts can assemble the microgels into a 3D MAP scaffold. Usually, spherical or rod-shaped microgels are chemically interlinked [5,42], resulting in 3D constructs with a fixed framework that limits cellular self-organization. Therefore, we recently investigated how cells can build such scaffolds without chemical interlinking, based on the cell-induced interlinking of biobased spherical microgels [36]. Different scaffold geometries were produced by these cells depending on the ratio of cells to microgels, the microgel stiffness, and the presence of cell-adhesion peptides on the microgels. Here, we selected the eight-arm sPEG-Ac microgels for assembly into 3D constructs based on the experiments where cells were seeded on top of the microgels (Fig. 7a). As no significant difference was observed in interactions between cells and the 10-kDa and 20-kDa eight-arm sPEG-Ac microgels (Fig. 7a), we selected the softer microgels for subsequent experiments because this reduces the amount of synthetic material required and maximizes diffusion.

To produce MAP scaffolds, GRGDSPC-modified microgels (12 microgels μL^{-1}) were seeded with 1000–2500 cells μL^{-1} (300,000–500,000 cells in total) on a PDMS-coated well plate, which prevents cells from attaching to the well surface and thus supports the formation of 3D constructs. The microgels and cells were co-incubated for 7 days and the resulting cellular constructs are shown in Fig. 7b. Reliable quantitative analysis was ensured by staining the microgels and cells with two different immunofluorescent dyes. The total actin surface area and actin volume of the 3D cell/microgel assemblies were higher when we added more cells (Fig. 7c–f), although the difference between 350,000 and 500,000 cells was not significant. Interestingly, the cell volume fraction (~78 %) was similar for all cell numbers, even though the higher cell numbers led to overall larger constructs, and the variability of these volume fractions was high, especially at higher cell numbers. The cell volume fraction obtained with rod-shaped microgels was slightly higher than with spherical microgels (~60–70 %) [36]. This suggests that MAP scaffolds prepared from rod-shaped microgels increase macroporosity due to the high aspect ratio of the microgels [5,6].

3. Conclusion

We have demonstrated, for the first time, that CJP-based microfluidics is suitable for the continuous production of ultra-thin or ultra-soft and ultra-porous rod microgels. The microfluidic design was adjusted to ensure sufficient photopolymerization enabling unique microgel properties. This expands the toolbox of material building blocks to produce more structured and denser 3D cellular constructs. Ultra-thin PEGDA microgels produced by CJP are ~20 times softer than the softest rod microgel prepared using PRINT. We established a protocol to post-functionalize the rod microgels with magnetic nanoparticles, resulting in magneto-responsive rods that align within ~5 s even in a weak magnetic field. Their positions and orientation can be fixed by a surrounding 3D hydrogel to form an Anisogel. Preliminary results indicate that the lower difference in stiffness between the rod microgel and the surrounding hydrogel matrix reduces cellular alignment compared to equivalent PRINT rods.

In addition to ultra-thin microgels, CJP was also used to produce ultra-soft rod microgels from sPEG-Ac, with large pores (2–5 μm). To enable cell-induced assembly of ultra-soft and ultra-porous microgels into MAP scaffolds, the microgels were post-modified with the cell-adhesion peptide GRGDSPC. Cell interactions with the microgels were dependent on the microgel's mechanical and structural properties. Only rod microgels prepared from eight-arm sPEG-Ac could be assembled by cells into large 3D MAP scaffolds. The fraction of cells found inside these 3D constructs was ~78 %, which is higher than when spherical microgels were used in a previous study [36]. CJP can therefore produce ultra-thin or ultra-soft and ultra-porous microgels that are suitable and customizable for a wide variety of tissue engineering applications. While the current throughput of our single-channel system is lower than

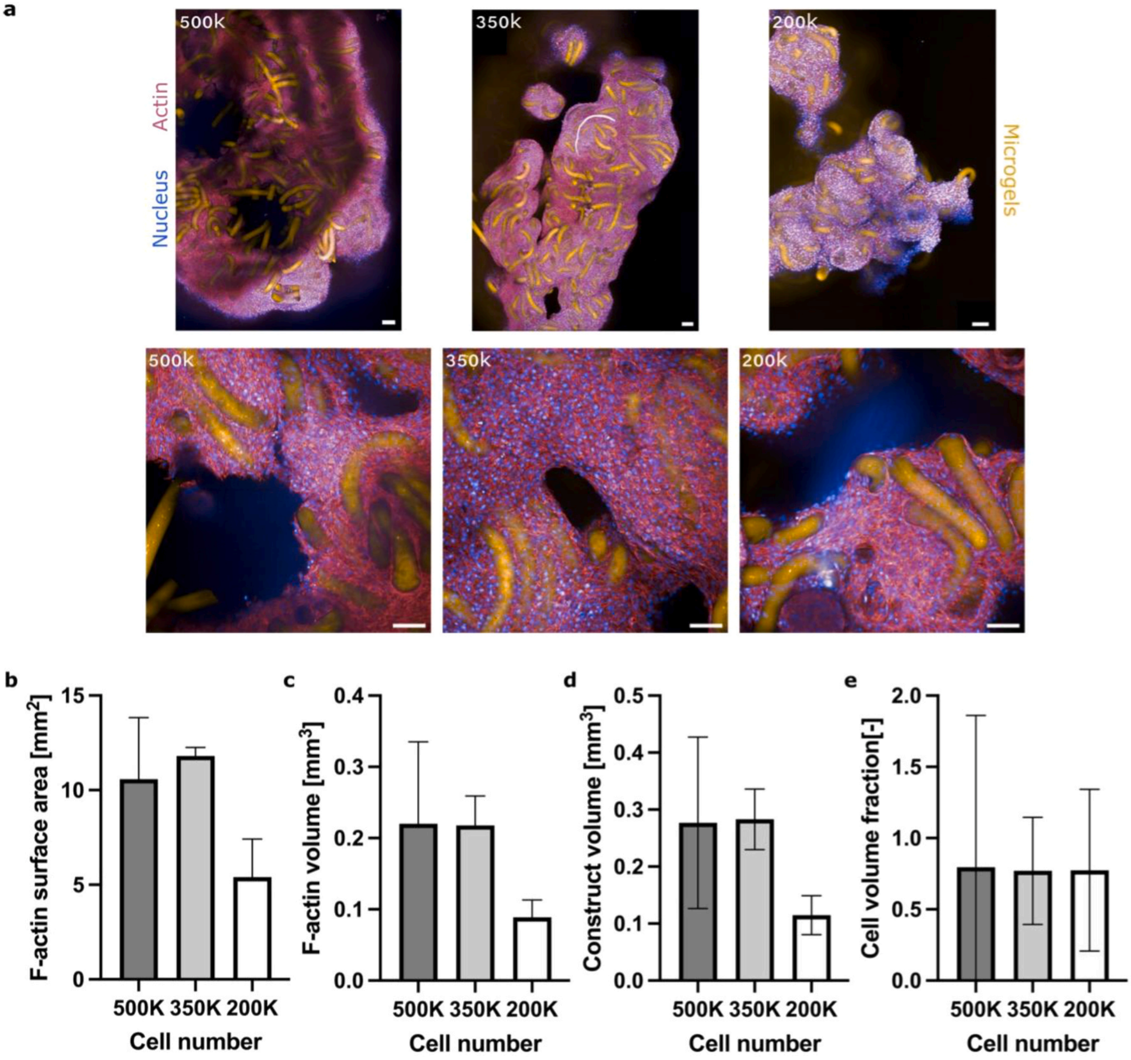

Fig. 7. Cell–microgel assembly. (a) Difference in microgel assembly: 3D cell-induced self-assembly of microgels with different numbers of L929 cells (500,000, 350,000 or 200,000) but a constant quantity of rod microgels. GRGDSPC-functionalized microgels were stained with Rhodamine B (orange), F-actin (red), and DAPI (cell nuclei, blue). Scale bars = 100 μm. (b–e) Effect of cell number on microgel assembly: Quantitative image analysis (Imaris) of 3D constructs displaying (b) F-actin surface area, (c) F-actin volume, (d) construct volume, and (e) cell volume fraction versus cell number. Data are means ± standard errors. (For interpretation of the references to colour in this figure legend, the reader is referred to the Web version of this article.)

PRINT, we are actively working on scaling strategies based on parallelization technologies. This could increase the continuous production rate of CJP to, for example, employ the microgels in automated pipetting systems to create *in vitro* tissue models.

4. Experimental section/methods

Preparation of PDMS-based microfluidic devices: Microfluidic chips were produced by soft lithography [8] using the SYLGARD 184 Silicone Elastomer Kit (Dow Silicones, Corning, NY, USA). The PDMS and curing agent were mixed at a 10:1 ratio. Unwanted irradiation outside the laser spot was prevented by dissolving 60 mg Oil Red (ThermoFisher Scientific, Waltham, MA, USA) and 3 mg Quinoline Yellow (ThermoFisher) in 2 g of toluene, and adding 1 % (w/w) of the dye solution to the mixture, which was placed in a desiccator under vacuum (10^{-3} mbar) to remove air. The mixture was then cast in the mold and the air was evacuated again in the desiccator. The PDMS was cured in an oven for 10 min at 110 °C and left in a sealed Petri dish at room temperature overnight to complete the crosslinking process. The cured PDMS was cut out and the inlet and outlet holes were created using a biopsy puncher with an inner diameter (ID) of 0.75 mm. The PDMS form was washed three times with isopropanol and water and dried under nitrogen gas. A glass microscope slide (75 × 50 × 0.13 mm; Carl Roth, Karlsruhe, Germany) was rinsed three times with acetone and isopropanol. The PDMS replica and glass slide were then bonded in a 100E oxygen plasma oven (PVA TePla, Wettenberg, Germany) at an oxygen flow rate of 25–27 mL $\min^{-1}$ and a pressure of 0.2 mbar for 40 s at 100 W, followed by baking for 3 h at 60 °C to complete the adhesion. A hydrophobic surface coating was applied to the microfluidic channels by silanization with 97 % tridecafluoro-1,1,2,2-tetrahydrooctyl-trichlorosilane (Sigma-Aldrich, St Louis, MO, USA). The microfluidic device was placed in a desiccator with the silane and evacuated overnight, and excess silane on the surface was removed using paraffin oil (VWR-Chemicals, Radnor, PA, USA).

Preparation of pre-polymer solutions: The pre-polymer solutions were prepared in brown glass vials to prevent photo-initiation. Four- or eight-arm PEG-acrylate (molecular weight = 10 or 20 kDa) (JenKem Technology USA Inc., Plano, TX, USA) or PEGDA (700 Da) (Sigma-Aldrich) were dissolved at concentrations of 3–40 % (w/w) in an aqueous 3 % (w/w) solution of non-reactive PEG (400 kDa) (Sigma-Aldrich) filler to obtain an end mass of 2000 mg. We added 1 % (w/w) LAP (Sigma-Aldrich) as a photo-initiator and 1 μL methacryloxyethyl thiocarbamoyl rhodamine B (Polysciences, Warrington, PA, USA) solution (10 mg in

100 µL DMSO (Sigma-Aldrich)) to label the microgels.

Microgel production: Microgels were produced as previously described [8]. The microfluidic station comprised two Pump 11 Elite syringe pumps (Harvard Apparatus, Holiston, MA, USA) and a DM IL LED inverted microscope (Leica Microsystems, Wetzlar, Germany) equipped with a Point Grey Fl3-U3-12Y3M − C camera (FLIR Systems, Wilsonville, OR, USA). The polymer solution and oil phase were injected using 1-mL or 5-mL gastight 1000 series syringes (Hamilton, Bonaduz, Switzerland) connected via polytetrafluorethylene (PTFE) tubing (BOLA S 1810–06, AD 0.9 mm × ID 0.400 mm; TECHLAB, Blacksburg, VA, USA). The syringe containing the pre-polymer solution was covered with aluminum foil and the microgels were collected in a protein LoBind tube (Eppendorf, Hamburg, Germany) filled with ethanol. A laser diode is used, that can be found in blue ray disc drives (Pioneer BDR-207 DBK). The dismounted diode is used at a power ranging from 25 to 150 mW. A single aspheric lens (Ø = 6.33 mm, focal length 4.02 mm) placed inside a M9x0.5 lens holder with adjustable focus is needed to focus the laser beam. The laser is mounted onto the microscope stage to provide illumination at 405 nm and an angle of ~45° to the sample surface, in a plane perpendicular or parallel to the microfluidic channel. Parallel positioning of the laser spot resulted in longer microgels due to the oval shape of the laser spot (~115 × 60 µm). The power was set to 50 mW, and confirmed using a PM200 optical power and energy meter with a S302C sensor (Thorlabs, Newton, NJ, USA). The laser light polarization plane was adjusted to minimize reflection from the glass surface. Custom electronics based on Arduino DUE (Arduino, Milan, Italy) and custom software was used to generate laser pulses. The laser on-time was varied from 250 µs to 50 ms and the off-time was the on-time plus 50 ms to ensure separation of the rod microgels. Longer irradiation times generate longer rod microgels at a constant velocity. Both the exposure time and the velocity determine the width and length of the rod microgels [8]. The microgels were collected inside a LoBind Eppendorf tube filled with ethanol (99.8 %, VWR-Chemicals) and were purified by five rounds of centrifugation with ethanol and three with water (5000 rpm, 10 min using an Eppendorf 5810 R centrifuge). All bright-field images were recorded on an AE2000 inverted microscope (Motic, Barcelona, Spain) using a 10 × objective equipped with a Point Grey Fl3-U3-12Y3M − C camera.

Numerical simulation: Ansys Fluent 2023 R1 (Ansys, Canonsburg, PA, USA) was used for all numerical simulations of fluid flow inside the microfluidic channel. This software uses the finite volume method to solve the governing equations numerically. The fluids inside the microchannel were considered incompressible. Isothermal and laminar flow conditions were imposed, and a maximum root mean square (RMS) residual error of 10^{-5} was chosen for continuity and momentum equations and 10^{-4} for volume fraction equations. The volume of fluid (VoF) model was used for multiphase fluid flow. The physical properties of both phases (oil and polymer) were set based on experimental measurements. A grid study ensured the use of proper element sizes. Additional details of numerical modeling and simulation are provided in Supplementary Information Section 4, Fig. S4 and Table S3.

Confocal microscopy of jet microfluidics: The pre-polymer solution was prepared as described above but without an initiator, and the oil phase was dyed with 99 % Cumarin 153 (Sigma-Aldrich). The samples were imaged using an SP8 tandem confocal microscope fitted with a 10 × /0.3 NA air objective (Leica Microsystems). Z-stacks 200–250 µm thick were acquired for each sample. Images were captured at the appropriate excitation wavelengths and the emission signals were captured using hybrid detectors or photomultipliers, as appropriate. Images were processed and 3D reconstructions of the jet were prepared from confocal images using specific plugins provided by Fiji [43]. We first adjusted the brightness and contrast of each channel (red = polymer, green = oil) to optimize the visualization of the jet structure and then merged both channels in each z-stack position. We then used the “3D viewer” plugin to reconstruct the 3D images.

Prussian blue staining protocol: Microgels were incubated with 5 % (w/v) potassium hexacyanoferrate (II) (MORPHISTO, Offenbach am Main, Germany) for 5 min at 40 °C. To the mixture an equal volume of 5 % (v/v) HCl (MORPHISTO) was added to react at 40 °C for 30 min. The microgel suspension was purified by centrifugation with distilled water as described above, and images were captured by fluorescence microscopy using a DM RX instrument (Leica Microsystems).

Magnetic functionalization of rod microgels and verification of magnetic alignment: For the *in situ* functionalization either EMG700 (Ferrotec, Bedford, NH, USA) or PBG300 (Ferrotec) SPIONs were added in the desired concentration to the pre-polymer solution.

To post-functionalize, the microgels were mixed with a solution containing 1 % (w/w) LAP and 200–600 µg ml^{-1} PEGMA SPIONs (micromod Partikeltechnologie, Rostock, Germany) and were then exposed to a custom LED in the UV range (λ = 365, spot diameter ~4.7 mm, ~135 mW cm^{-1}) for 10 min. The commercially custom-made magnetic nanoparticles exhibited a zetapotential −0.7 mV. Based on previous research [44], the presence of methacrylate groups was confirmed through UV absorption at 225 nm.

The quantity of nanoparticles was calculated relative to the microgel volume in the microgel dispersion to keep the microgel volume constant. The microgels were then purified by centrifugation with ultrapure water three times (5000 rpm, 10 min, Eppendorf 5810 R centrifuge). The magnetic response was tested by pipetting a small droplet onto a glass slide exposed to a magnetic field of 70 mT.

Sterilization of rod microgels: Before cell experiments, the (magneto-responsive) rod microgels were sterilized by immersing them in ethanol and exposing them to UV light for 1 h. Afterwards, they were purified by centrifugation with ultrapure water as above, and stored in ultrapure water at 4 °C.

Matrix hydrogel preparation: The PEG hydrogel was prepared as previously described [2,45]. Briefly, two separate batches of eight-arm star PEG-vinyl sulfone (sPEG-VS, 20 kDa; JenKem Technology) were conjugated with peptide solutions in triethanolamine, pH 8 (Sigma-Aldrich). The peptide sequences were H-NQEQVSPLERCG-NH_2 (Q-peptide; 1358.6 Da, Biosynth, Lelystad, NL and Ac-FKGGGPQGIWGQERCG-NH_2 (K-peptide; 1717.6 Da, Biosynth). Conjugation to cysteine residues involved Michael-type addition by incubating the solutions for 2 h at 37 °C. The solutions were then dialyzed for 4 days against water at 4 °C to remove any unreacted peptides. The solutions were lyophilized, dissolved in water, UV sterilized, and stored at −20 °C until further use. For gel preparation, equimolar amounts of the two PEG conjugates were mixed at a total concentration of 1.25 % (w/v) in cell culture medium, along with a 10 × calcium buffer (0.1 M $CaCl_2$, 0.5 M Tris, 1.1 M NaCl (Sigma-Aldrich)), 1 % (v/v) of the rod microgels, and 600 µM of the cell adhesion peptide GRGDSPC (CPC Scientific, Milpitas, CA, USA), as well as L929 mouse fibroblasts (passage 8–12, (Deutsche Sammlung von Mikroorganismen und Zellenkulturen GmbH, DSMZ ACC-2) (700 cells μL^{-1}). Gelation was initiated by adding 1250 U FXIIIa (CSL Behring, King of Prussia, PA, USA), which was activated by diluting 200 U mL^{-1} thrombin (Sigma–Aldrich) to 20 U mL^{-1} in a buffer (25 mM $CaCl_2$, 10 mM Tris, 150 mM NaCl) and incubating with the FXIII pro-enzyme for 30 min at 37 °C, shaking gently every 5 min. The FXIIIa was then aliquoted and stored at −80 °C until further use. The hydrogel mix was pipetted in 15-µL droplets into 15-well ibidi plates and flipped to ensure the distribution of the microgels in three dimensions. A self-made magnetic holder was placed around the plate, with opposing magnets creating a field of ~70 mT across the hydrogel droplets. The hydrogels were flipped back after 5 min and incubated at 37 °C in a 5 % CO_2 atmosphere to complete the gelation. The magnets were removed and 45 µL of Dulbecco’s modified Eagle’s medium (DMEM, Gibco, Thermo Fisher Scientific) supplemented with 10 % fetal bovine serum (FBS; Gibco or Biowest, Nuaillé, France) and 1 % antibiotics/mycotics (AMB; Gibco), and incubated for 7 days at 37 °C in a 5 % CO_2 atmosphere.

Immunostaining of hydrogel samples and cells: After 7 days in culture, the samples were washed twice with phosphate-buffered saline (PBS, pH = 7.4, c = 1 × , Thermo Fisher Scientific) and the cells were fixed with 4 % paraformaldehyde (Sigma-Aldrich) for 30 min (3D: 1h) at room temperature, followed by washing twice with PBS for 10 min (3D: 30 min), 0.1 % (v/v) Triton X-100 (Sigma-Aldrich) for 10 min (3D: 30 min) and PBS for 10 min (3D: 30 min). F-actin filaments were stained using phalloidin-633 diluted 1:1000 (Abcam, Cambridge, UK) in 4 % bovine serum albumin (BSA) in PBS for 1 h (3D: 4 h), followed by washing with PBS three times. Cell nuclei were stained using 4′,6-diamidino-2-phenylindole (DAPI) (Thermo Fisher Scientific) diluted 1:100 in PBS for 20 min (3D: 20 min), followed by with PBS. The samples were washed three times with PBS for 10 min and stored at 4 °C. The stained cells were imaged using an Opera Phenix Plus High-Content Screening System (PerkinElmer, Shelton, CT, USA) with 10 × /0.3 NA or 20 × /1.0 NA air objectives. Z-stacks with a z-gap of 7.4 (10 × objective) or 3.6 μm (20 × objective) were recorded for each sample. For quantification of the 3D MAP constructs, the z-stacks were converted to Imaris file format using Imaris File Converter v9.91 and stitched together with Imaris Stitcher. The images are analyzed with Imaris v10.0 software (Oxford Instruments, Oxford, UK) by creating 3D volume renderings of the F-actin stained structures, as well as Rhodamine B stained microgels, using the surface rendering module with individually selected thresholds. To exclude unwanted structures in the cell volume, structures with a voxel number <100 were omitted. To investigate the influence of cell/microgel ratios, we quantified the construct volume, F-actin area and F-actin volume, and microgel volume. The cell volume fraction was quantified as a fraction of the sum of microgels and F-actin (cell) volume resulting in the total construct volume.

Analysis of microgel and cellular alignment: Microgel and cell images obtained by laser scanning confocal fluorescence microscopy were analyzed using a python program [46] as described in more detail in the Supplementary Information Section 9.

Rheology measurements: Rheological characterization was carried out using a Discovery HR-3 hybrid rheometer (TA Instruments, New Castle, DE, USA) with 20-mm parallel plate geometry. We transferred 381 μL of the pre-polymer solution to the rheometer at 25 °C followed by the time-dependent measurement of polymerization under 10 mW cm^{-2} UV light with a frequency of 1 Hz and an oscillation strain of 1 %. We also took frequency-dependent measurements at a set oscillation strain of 1 % and strain-dependent measurements at a set frequency of 1 Hz. Each material was measured as triplicate samples.

Stiffness of microgels determined by AFM: AFM point force spectroscopy was carried out using a Dimension Icon AFM (Bruker, Billerica, MA, USA) and a CP-PNPL-PS-D-5 colloidal probe (NanoAndMore, Wetzlar, Germany) with a nominal diameter of ~2 μm. The force probe was mounted on a liquid probe holder glass prism. Samples were measured in the lid of a 3-cm diameter Petri dish containing water to a height of ~1 mm. Force curves were measured with an approach and retraction speed set to 1 μm s^{-1}, and a waiting time of 100 ms at contact. The maximum relative force was set to 4 nN. All curves were exported as ASCII files. The approach part of the curves was analyzed using the custom script AFMIndentation [47] in Python [48] based on the Hertz model (Equation (1)). The Poisson ratio was assumed to be that of an incompressible material ($\nu = 0.5$). The last 20 % of the data points were fitted to a line and subtracted as background.

$$F(\delta) = \frac{4}{3}\,\frac{E}{1-\nu^2}\,\sqrt{R}(\delta-\delta_0)^{3/2} \tag{1}$$

The model was fit up to a force of 2 nN, practically the whole force range of the curve using a nonlinear fit (leastsq() from Scipy [49]) finding both the Young's modulus and the contact point. At least three microgels (N > 3) were indented per condition and an average of all the indentation results per microgel was calculated as its Young's modulus. The effective radius for microgels with 2.5 μm diameter is about 0.55 μm.

Porosity analysis: A TCS SP8 3X confocal microscope (Leica Microsystems) with an 86 × /1.2 NA water immersion objective (Leica HC PL APO CS2-STED White) was used to examine microgels labeled with Rhodamine B (Polysciences, Warrington, PA, USA) embedded inside a hydrogel. The excitation wavelength was set to 541 nm and the detection band was restricted to 560–700 nm with a multiband spectrophotometer in front of a HyD hybrid detector (Leica Microsystems). All images were captured at a room temperature (22.5 °C) in a 1024 × 1024 pixel format with 20 nm pixel size. Images were processed using a custom python script [48] based on ImageP [50]. Images were sharpened by removing off-plane light with background correction. Background was calculated by convolving images with a somewhat flattened Gaussian kernel using a standard deviation of 10 pixels, but truncated to a window size of 41 pixels (normalized to its sum). Then this background was subtracted, and negative intensity values were set to zero. The resulting image was smoothened by convolving it with another Gaussian kernel (standard deviation of 1 pixel, window size 7 pixels) then converted to a binary image cut with a threshold determined using Otsu's method [51]. The identified pores were skeletonized based on a distance transform, where local maxima were identified with a minimum step size of 1 (intensity difference between neighbors). Because the distance transform sets the pixels to the square of their Euclidian distance from the nearest edge pixel, the double of the square root of the maximum pixels provides a local size measure of the pores. These values were collected and used to build histograms of the distances within the image.

Z-stack comparisons were generated from the exported pore size lists using R [version 4.5.2, R Foundation for Statistical Computing, https://cran.r-project.org/]. The tables were analyzed for the mean, median and standard deviation and histogram of the size population at every Z-slice. These then used to generate comparison how the pores changed at the various Z-positions. The corresponding R file has been added as a supplementary file.

Brillouin microscopy: Brillouin frequency shift maps were acquired using a confocal configuration for acoustic phonon excitation and signal detection, and a Brillouin spectrometer consisting of a two-stage virtually imaged phase array (VIPA) etalon, as previously described [52]. Briefly, the sample was illuminated with a frequency-modulated diode laser beam ($\lambda = 780.24$ nm, DLC TA PRO 780; Toptica, Munich, Germany). The laser light was coupled into a single-mode fiber and directed into the side port of an Axio Observer 7 inverted microscope stand (Carl Zeiss, Jena. Germany), where an objective lens (20 × /0.5 NA, EC Plan-Neofluar; Carl Zeiss) illuminated the focused laser beam on the sample mounted on a motorized microscope stage. The backscattered light from the sample was collected by the same objective lens and coupled into the second single-mode fiber to achieve confocality before delivery to the Brillouin spectrometer. In the Brillouin spectrometer, two VIPA etalons (OP-6721-6743-4; Light Machinery, Ottawa, Canada) with the free spectral range of 15.2 GHz converted the frequency shift of the light into the angular dispersion in the Brillouin spectrum, which was acquired by a sCMOS camera (Prime BSI; Teledyne, Thousand Oaks, CA, USA) with an exposure time of 0.5 s per measurement point. The two-dimensional Brillouin frequency map of the sample was created by scanning the *x*–*y* motorized microscope stage with a translational step size of 0.5 μm. The Brillouin microscope was controlled with custom acquisition software written in C++ [53] and the Brillouin frequency shift was evaluated using custom software [54].

Optical diffraction tomography: The RI distribution of microgel rods was assessed by ODT, which uses Mach-Zehnder interferometry to capture multiple complex optical fields from diverse incident angles [55]. A solid-state laser beam ($\lambda = 532$ nm, 50 mW; CNI Optoelectronics Technology, Changchun, China) was split into two paths, one serving as a reference beam and the other illuminating the sample on the stage of an Axio Observer 7 inverted microscope via a tube lens (f = 175 mm) and a water-dipping objective lens (40 × /1.0 NA; Carl Zeiss). The diffracted beam from the sample was collected by a water immersion objective lens (63 × /1.3 NA; Carl Zeiss). We reconstructed 3D RI tomograms by illuminating the sample from 150 incident angles and scanning with a dual-axis GVS212/M galvanomirror (Thorlabs) aligned with the conjugate plane of the sample. The diffracted beam interfered with the reference beam at an image plane, generating a spatially modulated hologram that was recorded using a CMOS camera (MQ042MG-CM-TG; XIMEA, Münster, Germany) with a field-of-view covering 173.6 × 173.6 μm. Complex optical fields were extracted from the recorded holograms using a Fourier transform-based field retrieval algorithm. The 3D RI distribution of the samples was then reconstructed using Fourier diffraction theorem with first-order Rytov approximation [56,57] as described in detail elsewhere [58]. We used a MATLAB script for ODT reconstruction [59].

Small-angle X-ray scattering: SAXS experiments were carried out using beamline KWS-X (XENOCS XUESS 3.0 XL) at JCNS MLZ [60]. The X-ray source is a D2+ MetalJet (Excillum, Kista, Sweden) with a liquid metal anode operating at 70 kV and 3.57 mA with Ga-Kα radiation (wavelength $\lambda = 1.314$ Å). Samples were analyzed in a glass capillary (2 mm ID) at room temperature (25 °C). The sample-to-detector distances were 0.5 m and 1.7 m, which covered a scattering vector q range of 0.002–1.1 $Å^{-1}$. Q is the scattering vector, where $Q = (4\pi/\lambda)\sin(\theta)$, and 2θ is the scattering angle. The SAXS patterns were normalized to an absolute scale and azimuthally averaged to obtain intensity profiles, from which the solvent background was subtracted.

Cell culture: L929 mouse fibroblasts were cultured in DMEM supplemented with 10 % FBS and 1 % antibiotics and mycotics at 37 °C in a humidified 5 % CO_2 atmosphere, as described above. For cell culture experiments, glass-bottom plates were coated with sterile PDMS using the SYLGARD184 Silicone Elastomer Kit as described above, and crosslinked at 60 °C for 90 min. A droplet of microgel suspension (20 μL) was transferred to the PDMS and sedimented for 1 h. The well plates were filled up with media then seeded with L929 fibroblasts at a concentration of 200 cells μL^{-1}. The cells were cultivated for 7 days as described above.

Diffusion experiment: A water-based solution consisting of FITC-dextran (0.05 mM, 500 kDa, Sigma-Aldrich) was prepared and mixed with the Rhodamin B labeled microgels. Confocal images were recorded using a SP8 tandem confocal microscope fitted with a 10 × /0.3 NA air objective (Leica Microsystems). Z-stacks of 200–250 μm thick were acquired for each sample. Images were captured at the appropriate excitation wavelengths (561 nm Rhodamin B and 488 nm FITC-dextran) and the emission signals were captured using hybrid detectors or photomultipliers, as appropriate.

Statistical analysis: All data points are means with error bars indicating standard deviations with a sample size of at least 3, or as otherwise stated in the text. Statistical significance was determined by one-way or two-way analysis of variance (ANOVA) with Tukey's or Holm-Sidak's multiple comparisons test. Statistical tests were carried out using GraphPad Prism v10 (GraphPad Software, Boston, MA, USA) and significance was indicated as follows: $^{*}p < 0.05$, $^{**}p < 0.01$, $^{***}p < 0.001$, and $^{****}p < 0.0001$.

CRediT authorship contribution statement

Ninon Möhl: Writing – review & editing, Writing – original draft, Visualization, Validation, Methodology, Investigation, Formal analysis. **Susan Babu:** Writing – review & editing, Validation. **Camille Bonhomme:** Validation. **Ramin Nasehi:** Writing – review & editing, Visualization, Investigation. **Matthias Mork:** Writing – review & editing, Visualization. **Tamás Haraszti:** Writing – review & editing, Formal analysis. **Gilles Wittmann:** Investigation, Formal analysis. **Baohu Wu:** Investigation, Formal analysis. **Rostislav Vinokur:** Writing – review & editing, Software. **Kyoohyun Kim:** Investigation, Formal analysis. **Rafael Kramann:** Writing – review & editing. **Jochen Guck:** Writing – review & editing. **Laura De Laporte:** Writing – review & editing, Supervision, Resources, Funding acquisition.

Data statement

The data supporting the findings of this study are available from the corresponding author upon reasonable request.

Declaration of competing interest

The authors declare that they have no known competing financial interests or personal relationships that could have appeared to influence the work reported in this paper.

Acknowledgments

We thank Nina Schöling (DWI – Leibniz Institute for Interactive Materials) for cell culture and hydrogel material preparation and Yonca Kittel and Dr. Andreas Krüger for valuable discussions. We also thank Tom Schneider and Laura Letan for their help during data acquisition. The analytical data for particle size, zeta potentials and UV spectrophotometric data were provided by micromod Partikeltechnologie GmbH. N.M. is supported by the Add-on Fellowship of the Joachim Herz Foundation. This work was supported by the High Content Screening Facility, a Core Facility of the Interdisciplinary Center for Clinical Research (IZKF) Aachen within the Faculty of Medicine at RWTH Aachen University, and by the immunohistochemistry facility of the Interdisciplinary Center for Clinical Research (IZKF) Aachen within the Faculty of Medicine at RWTH Aachen University. This research was conducted within the Max Planck School Matter to Life supported by the German Federal Ministry of Education and Research (BMBF) in collaboration with the Max Planck Society. This work was also funded by the German Research Foundation (DFG, Deutsche Forschungsgemeinschaft) project 363055819/GRK2415 (ME3T), and clinical research unit 5011 InteraKD (project 445703531), the European Research Council (ERC-2021-COG project 101043656, Heartbeat), and the European Research Council HORIZON-ERC-POC project 101150675, AnisoPlate. We acknowledge the support of the Government of Canada#8217; s New Frontiers in Research Fund (NFRF), [NFRFT-2020-00238], within the project Mend the Gap. This work was also supported by the Werner Siemens Foundation.

Appendix A. Supplementary data

Supplementary data to this article can be found online at https://doi.org/10.1016/j.biomaterials.2025.123866.

Data availability

Data will be made available on request.

References

[1] S. Babu, et al., How do the local physical, biochemical, and mechanical properties of an injectable synthetic anisotropic hydrogel affect oriented nerve growth? Adv. Funct. Mater. 32 (50) (2022) 2202468.
[2] C. Licht, et al., Synthetic 3D PEG-anisogel tailored with fibronectin fragments induce aligned nerve extension, Biomacromolecules 20 (11) (2019) 4075–4087.
[3] J.C. Rose, et al., Biofunctionalized aligned microgels provide 3D cell guidance to mimic complex tissue matrices, Biomaterials 163 (2018) 128–141.
[4] D.R. Griffin, et al., Accelerated wound healing by injectable microporous gel scaffolds assembled from annealed building blocks, Nat. Mater. 14 (7) (2015) 737–744.
[5] D. Rommel, et al., Functionalized microgel rods interlinked into soft macroporous structures for 3D cell culture, Adv. Sci. (Weinh.) 9 (10) (2022) e2103554.
[6] A.C. Suturin, et al., Annealing high aspect ratio microgels into macroporous 3D scaffolds allows for higher porosities and effective cell migration, Adv. Healthcare Mater. 11 (24) (2022) 2200989.
[7] J.C. Rose, et al., Nerve cells decide to orient inside an injectable hydrogel with minimal structural guidance, Nano Lett. 17 (6) (2017) 3782–3791.
[8] A.J. Krueger, et al., Compartmentalized jet polymerization as a high-resolution process to continuously produce anisometric microgel rods with adjustable size and stiffness, Adv. Mater. 31 (49) (2019) 1903668.
[9] A.J.D. Krüger, et al., Compartmentalized jet polymerization as a high-resolution process to continuously produce anisometric microgel rods with adjustable size and stiffness, Adv. Mater. 31 (49) (2019) 1903668.
[10] L. Steinbeck, et al., Magnetically actuable complex-shaped microgels for spatio-temporal flow control, Adv. Mater. Technol. 8 (14) (2023) 2300044.

[11] D. Dendukuri, et al., Stop-flow lithography in a microfluidic device, Lab Chip 7 (7) (2007) 818–828.

[12] D. Dendukuri, et al., Modeling of oxygen-inhibited free radical photopolymerization in a PDMS microfluidic device, Macromolecules 41 (22) (2008) 8547–8556.

[13] K. Krutkramelis, B. Xia, J. Oakey, Monodisperse polyethylene glycol diacrylate hydrogel microsphere formation by oxygen-controlled photopolymerization in a microfluidic device, Lab Chip 16 (8) (2016) 1457–1465.

[14] A.K. O'Brien, C.N. Bowman, Modeling the effect of oxygen on photopolymerization kinetics, Macromol. Theory Simul. 15 (2) (2006) 176–182.

[15] C. Decker, A novel method for consuming oxygen instantaneously in photopolymerizable films, Makromol. Chem.: Macromol. Chem. Phys. 180 (8) (1979) 2027–2030.

[16] C. Decker, J. Faure, L. Rychia, Elimination of Oxygen Inhibition in Photopolymerization, 1979.

[17] C.W. Miller, et al., *N-vinylamides and reduction of oxygen inhibition in photopolymerization of simple acrylate formulations*, in *photointiated polymerization*, in: ACS Symposium Series, 2003, pp. 2–14.

[18] V.V. Krongauz, C.P. Chawla, J. Dupre, Oxygen and Radical Photopolymerization in Films, 2003.

[19] P. Panda, et al., Stop-flow lithography to generate cell-laden microgel particles, Lab Chip 8 (7) (2008) 1056–1061.

[20] J.C. Rose, et al., How much physical guidance is needed to orient growing axons in 3D hydrogels? Adv. Healthcare Mater. 9 (21) (2020) 2000886.

[21] C.M. Hwang, et al., Benchtop fabrication of PDMS microstructures by an unconventional photolithographic method, Biofabrication 2 (2010) 045001.

[22] L.R. Kuck, A.W. Taylor, Photopolymerization as an innovative detection technique for low-density microarrays, Biotechniques 45 (2) (2008) 179–182, 184-182.

[23] R.M. Olabisi, et al., Hydrogel microsphere encapsulation of a cell-based gene therapy system increases cell survival of injected cells, transgene expression, and bone volume in a model of heterotopic ossification, Tissue Eng. 16 (12) (2010) 3727–3736.

[24] J.R. Nair, et al., UV-Induced radical photo-polymerization: a smart tool for preparing polymer electrolyte membranes for energy storage devices, Membranes 2 (4) (2012) 687–704.

[25] J. Mandal, K. Zhang, N.D. Spencer, Oxygen inhibition of free-radical polymerization is the dominant mechanism behind the "mold effect" on hydrogels, Soft Matter 17 (26) (2021) 6394–6403.

[26] J.A. Conchello, J.W. Lichtman, Optical sectioning microscopy, Nat. Methods 2 (12) (2005) 920–931.

[27] D.L. Braunmiller, et al., Pre-programmed rod-shaped microgels to create multi-directional anisogels for 3D tissue engineering, Adv. Funct. Mater. 32 (50) (2022) 2202430.

[28] A. Omidinia-Anarkoli, et al., An injectable hybrid hydrogel with oriented short fibers induces unidirectional growth of functional nerve cells, Small 13 (36) (2017) 1702207.

[29] R.M. Erb, et al., Composites reinforced in three dimensions by using low magnetic fields, Science 335 (6065) (2012) 199–204.

[30] J.C. Rose, et al., Predicting the orientation of magnetic microgel rods for soft anisotropic biomimetic hydrogels, Polym. Chem. 11 (2) (2020) 496–507.

[31] B.V. Slaughter, et al., Hydrogels in regenerative medicine, Adv. Mater. 21 (32–33) (2009) 3307–3329.

[32] Y. Kittel, A.J.C. Kuehne, L. De Laporte, Translating therapeutic microgels into clinical applications, Adv. Healthcare Mater. 11 (6) (2022) e2101989.

[33] N. Annabi, et al., Controlling the porosity and microarchitecture of hydrogels for tissue engineering, Tissue Eng., Part B 16 (4) (2010) 371–383.

[34] S. Bulut, et al., Tuning the porosity of dextran microgels with supramacromolecular nanogels as soft sacrificial templates, Small 19 (45) (2023) 2303783.

[35] A.J. Krüger, et al., A catalyst-free, temperature controlled gelation system for in-mold fabrication of microgels, Chem. Commun. 54 (50) (2018) 6943–6946.

[36] S. Bulut, et al., Cellular architects at work: cells building their own microgel houses, Adv. Healthcare Mater. 13 (2024) 2302957.

[37] Y. Kittel, et al., Varying the stiffness and diffusivity of rod-shaped microgels independently through their molecular building blocks, Angew Chem. Int. Ed. Engl. 62 (44) (2023) e202309779.

[38] R. Schlüßler, et al., Correlative all-optical quantification of mass density and mechanics of subcellular compartments with fluorescence specificity, eLife 11 (2022) e68490.

[39] Z. Meng, et al., Assessment of local heterogeneity in mechanical properties of nanostructured Hydrogel networks, ACS Nano 11 (8) (2017) 7690–7696.

[40] E.A. Cavalcanti-Adam, et al., Lateral spacing of integrin ligands influences cell spreading and focal adhesion assembly, Eur. J. Cell Biol. 85 (3) (2006) 219–224.

[41] M. Arnold, et al., Induction of cell polarization and migration by a gradient of nanoscale variations in adhesive ligand spacing, Nano Lett. 8 (7) (2008) 2063–2069.

[42] N.F. Truong, et al., Microporous annealed particle hydrogel stiffness, void space size, and adhesion properties impact cell proliferation, cell spreading, and gene transfer, Acta Biomater. 94 (2019) 160–172.

[43] J. Schindelin, et al., Fiji: an open-source platform for biological-image analysis, Nat. Methods 9 (7) (2012) 676–682.

[44] X.-S. Chai, F.J. Schork, E.M. Oliver, ATR-UV monitoring of methyl methacrylate miniemulsion polymerization for determination of monomer conversion, J. Appl. Polym. Sci. 99 (4) (2006) 1471–1475.

[45] M. Ehrbar, et al., Biomolecular hydrogels formed and degraded via site-specific enzymatic reactions, Biomacromolecules 8 (10) (2007) 3000–3007.

[46] Gauss-edge.py Script. [cited 2024 08.09.2024]; Available from: https://github.com/tomio13/ImageP/blob/main/Example/Gauss-edge.py.

[47] AFM indentation script [cited 2024 08.09.2024]; Available from: https://github.com/tomio13/AFMforce/.

[48] Python [cited 2024 08.09.2024]; Available from: https://www.python.org.

[49] Scipy [cited 2024 08.09.2024]; Available from: https://www.scipy.org.

[50] Available from: https://github.com/tomio13/ImageP.

[51] N. Otsu, A threshold selection method from gray-level histograms, IEEE Trans. Syst. Man Cybern. 9 (1) (1979) 62–66.

[52] R. Schlüßler, et al., Mechanical mapping of spinal cord growth and repair in living zebrafish larvae by brillouin imaging, Biophys. J. 115 (5) (2018) 911–923.

[53] Brillouin acquisition [cited 2024 08.09.2024]; Available from: https://github.com/BrillouinMicroscopy/BrillouinAcquisition.

[54] BMicro [cited 2024 08.09.2024]; Available from: https://github.com/BrillouinMicroscopy/BMicro.

[55] K. Kim, J. Guck, The relative densities of cytoplasm and nuclear compartments are robust against strong perturbation, Biophys. J. 119 (10) (2020) 1946–1957.

[56] E. Wolf, Three-dimensional structure determination of semi-transparent objects from holographic data, Opt. Commun. 1 (4) (1969) 153–156.

[57] Y. Sung, et al., Optical diffraction tomography for high resolution live cell imaging, Opt. Express 17 (1) (2009) 266–277.

[58] K. Kim, et al., High-resolution three-dimensional imaging of red blood cells parasitized by Plasmodium falciparum and in situ hemozoin crystals using optical diffraction tomography, J. Biomed. Opt. 19 (1) (2014) 011005.

[59] ODT reconstruction [cited 2024 08.09.2024]; Available from: https://github.com/OpticalDiffractionTomography/ODT_Reconstruction.

[60] Saxs [cited 2024 10.02.2024]; Available from: https://mlz-garching.de/saxs-lab.